Journal of Molecular Structure 1360 (2026) 145576

Contents lists available at ScienceDirect

Journal of Molecular Structure

journal homepage: www.elsevier.com/locate/molstr

Kojibiose as a sustainable bioactive molecule: Experimental and DFT insights into antibacterial activity and electronic properties

Jeffrin JA Laura [a], P. Rajesh [a,*], S. Kayashrini [a], S Bala Abirami [b]

[a] Department of Physics, School of Basic Sciences, Vels Institute of Science, Technology & Advanced Studies, Pallavaram, Chennai, 600117 Tamil Nadu, India
[b] Department of Condensed Matter Physics, Saveetha School of Engineering, Saveetha Institute of Medical and Technical Sciences (SIMATS), Chennai, 602105 Tamil Nadu, India

ARTICLE INFO

Keywords:
B3LYP/6-311++G(d,p)
NLO
Antibacterial
PED
HOMO-LUMO

ABSTRACT

In this work, the structural, electronic, vibrational, and biological properties of Kojibiose (KB), a naturally occurring disaccharide, were assessed using a combination of experimental and computational methods. The molecular geometry was optimized by means of Density Functional Theory (DFT) calculations at the B3LYP/6-311++G(d,p) level, which yielded comprehensive information on bond lengths, bond angles, dihedral angles, and intramolecular hydrogen bonding interactions that stabilize the pyranose ring structure. Whereas NBO and HOMO-LUMO analyses demonstrated notable intramolecular charge delocalization and electronic stability, vibrational analyses, backed by FT-IR spectra and Potential Energy Distribution (PED), validated distinctive functional group frequencies. Significant nonlinear optical response was suggested by topological descriptors and NLO property calculations, including dipole moment, polarizability, and first-order hyperpolarizability, while UV-Visible spectral analysis revealed prominent electronic transitions, suggesting possible photophysical activity. Gram-positive Staphylococcus aureus and Gram-negative Escherichia coli were both effectively inhibited by antibacterial activity assessed using the agar well diffusion method, with inhibition zones that were comparable to those of common antibiotics. The combination of measurable bioactivity, stability, and strong electronic properties suggests that KB has promising multifunctional qualities appropriate for optoelectronic and pharmaceutical applications.

1. Introduction

The constant search for new treatment agents with enhanced efficacy and selectivity is fuelled by the fact that cancer is still one of the top causes of death globally. In addition to being a food additive and prebiotic, Kojibiose (KB) is an uncommon disaccharide made up of two glucose units connected by an α-(1→2) glycosidic bond. It has also lately attracted attention due to its possible biological and pharmaceutical uses. It is a stable, low-calorie sugar alternative that may have health benefits. It is naturally present in Gram-positive bacteria as a component of cell wall lipoteichoic acids. Notably, it has been discovered that KB specifically inhibits α-glucosidase I, an enzyme implicated in glycoprotein processing pathways that are frequently increased in viral infections and malignancies. The development of therapies derived from KB that may have anticancer properties is made possible by this inhibitory mechanism. With kinetic values (kcat = 1.1 s^{-1}, Km = 1.05 mM) that demonstrate strong biochemical recognition, KB demonstrated great specificity toward KB phosphorylase (YcjT) in enzymatic investigations, making it a suitable choice for drug-target modelling [1–3]. Additionally, KB shares structural similarities with derivatives of kojic acid, many of which have demonstrated specific cytotoxicity against colon, breast, ovarian, and liver cancer cell lines while sparing healthy cells. These results imply that KB has anticancer potential, either directly through biological activity or through processes of DNA binding and metal ion chelation [4,5]. Although KB exhibits encouraging biological properties, not much is known about how it interacts with biological systems at the molecular level. Previous studies on KB have mainly focused on its biochemical synthesis, enzymatic pathways, and nutritional relevance. However, reports addressing its electronic structure, nonlinear optical response, and structure–property correlation with antibacterial activity are absent. The present work bridges this gap by providing the first integrated experimental and DFT-based investigation linking the molecular electronics of KB with its biological and optoelectronic potential. In this work, we use a set of 6-311++ G(d,p) basis

* Corresponding author.
E-mail addresses: jeffrinlaura1998@gmail.com (J.J. Laura), rajesh.ncc5coy@gmail.com (P. Rajesh).

https://doi.org/10.1016/j.molstruc.2026.145576
Received 13 November 2025; Received in revised form 24 January 2026; Accepted 2 February 2026
Available online 3 February 2026

set and the B3LYP functional methods to analyse KB in detail. Its spectroscopic characteristics are better understood through the use of nuclear magnetic resonance (NMR) and ultraviolet-visible (UV-Vis) spectral simulations, while structural and dynamic information is provided by geometric optimization and vibrational assignments. Chemical stability and electron transport characteristics can be discovered by the use of Frontier Molecular Orbital (FMO) and Density of States (DOS) investigations, which include the HOMO–LUMO energy gap. Global Reactivity Descriptors (GRDs) and Molecular Electrostatic Potential (MEP) mapping are used to further describe electrophilic and nucleophilic locations. To investigate intra- and intermolecular interactions, bonding properties, and non-covalent interactions, sophisticated computational techniques like Natural Bond Orbital (NBO) analysis, Electron Localization Function (ELF) and Localized Orbital Locator (LOL) are used. The thorough computational approach used in this work advances our knowledge of KB at the molecular level and offers a solid basis for its possible use in the development of targeted therapies, including anticancer medications. This study's originality lies in the integration of experimental and DFT based analysis, establishing a connection between the molecule's electronic structure and its spectroscopic, nonlinear optical and antibacterial properties for the first time.

2. Experimental details

Without any additional purification, the pharmaceutical component KB was utilized after being purchased in powdered form from Sigma-Aldrich, a reputable chemical supplier. Using a Spectrum Two FT-IR Spectrometer (PerkinElmer) fitted with a $LiTaO_3$ detector, the title compound's Fourier Transform Infrared (FT-IR) spectrum was captured at room temperature. With a resolution of 0.5 cm^{-1}, the measurements were performed in the 4000–400 cm^{-1} spectral region. With the use of nuclear magnetic resonance (NMR) spectroscopy, the molecular structure was further verified. A Bruker 400 MHz NMR spectrometer was used to record the ^1H and ^{13}C NMR spectra in dimethyl sulfoxide (DMSO) as the solvent.Coupling constants (J) are expressed in Hertz (Hz), and chemical shifts (δ) are expressed in parts per million (ppm) with respect to tetramethylsilane (TMS) as an internal reference. A Shimadzu UV-1700 series spectrophotometer was used to measure the compound's ultraviolet-visible (UV-Vis) absorption spectra.The measurements were carried out with a scanning interval of 0.2 nm and in the wavelength range of 200–800 nm. The SRM College of Science in Kattankulathur, Tamil Nadu, India, provided all of the spectroscopic characterizations.

3. Computational details

For all quantum chemistry computations, the Gaussian 09 software was utilized [6]. Density Functional Theory (DFT) was used to fully optimize the target compound's molecular shape utilizing the 6-311++G(d,p) basis set and the B3LYP functional. GaussView 5.0.8 was used to see the Frontier Molecular Orbitals (HOMO–LUMO), the optimized molecular structure, and the Molecular Electrostatic Potential (MEP) map [7].The Potential Energy Distribution (PED) acquired from the VEDA 4.0 program was used to carry out the vibrational assignments, and the optimized geometry was further utilized to compute the vibrational wavenumbers [8].The Multiwfn program was used to perform reduced density gradient (RDG), localized orbital locator (LOL), and electron localization function (ELF) investigations in order to investigate the electronic structure and non-covalent interactions [9]. The Mulliken atomic charge distribution and Natural Bond Orbital (NBO) analysis were also calculated at the same theoretical level (B3LYP/6-311++G(d,p)). In addition, the compound's UV-visible absorption spectra were captured and examined between 200 and 400 nm in order to comprehend its electronic transitions. To construct the ligand and protein structures and assess the interaction modes at the active sites of certain protein targets, AutoDock Tools 1.5.6 (ADT) [10] was utilized for molecular docking experiments. Using Koopmans' approximation, the global reactivity descriptors were computed within the conceptual density functional theory framework. The following relations were used to assess the chemical hardness (η), chemical softness (σ) and electrophilicity index (ω).

$$\eta = \frac{E_{LUMO} - E_{HOMO}}{2}$$

$$\sigma = \frac{1}{\eta}$$

$$\omega = \frac{\mu^2}{2\eta}, \; where, \; \mu = \frac{E_{HOMO} + E_{LUMO}}{2}$$

These descriptors are widely used to assess molecular stability, chemical reactivity, and electrophilic character in DFT- based studies [11–13].

4. Result and discussion

4.1. Structural analysis

Structural optimization is essential to confirm the molecular stability and accurate geometry of KB. The KB molecule's molecular geometry was optimized at the B3LYP level using Density Functional Theory (DFT) and the 6–311++G(d,p) basis set. Table 1 displays the properties, which include bond lengths, bond angles, and dihedral angles. Fig. 1 shows the optimized molecular structure and the atom numbering system created with Gauss View [14,15]. Its stereo electrical arrangement, which consists of 74 bond angles and 75 bond lengths, is clearly visible. According to the optimal geometry table, the C–C bond lengths in KB are within the normal range for saccharides. C_3-C_5 = 1.54 Å, C_5-C_7 = 1.52 Å, and C_{13}-C_{14} = 1.53 Å, for example, all cluster about 1.52–1.55 Å, confirming the stability of the pyranose ring skeleton. The strength of the glycosidic and hydroxyl bonds in the disaccharide is confirmed by the C-O linkages, which likewise follow typical carbohydrate values: C_3-O_4 = 1.42 Å, C_5-O_6 = 1.41 Å, and C_9-O_{10} = 1.40 Å, respectively. As shown by O_6-H_{27} = 0.96 Å, O_{10}-H_{31} = 0.97 Å, and O_{15}-H37 = 0.96 Å, the O-H bonds regularly occur close to 0.97 Å, confirming the correct geometry of hydroxyl groups. Similar to this, C-H bonds are kept within predicted ranges, such as C_2-H_{24} = 1.09 Å, C_3-H_{25} = 1.09 Å, and C_{14}-H_{36} = 1.10 Å. Most of the angles in the KB bond angle dataset fall within the typical 109–113° range that characterizes sp^3-hybridized carbons. For instance, the tetrahedral geometry is well aligned with C_5-C_7-C_9 = 111.46°, O_8-C_7-C_9 = 113.43°, and C_7-O_8-H_{29} = 107.49°. Similarly, the sp^3 arrangement at carbon centres is further confirmed by O_1–C_9–O_{10} = 111.82° and O_{10}–C_9–C_{11} = 109.28°. Weak through-space interactions are shown by long intramolecular contacts as O_1-C_{11} (2.35 Å), O_1-O_{12} (2.82 Å), and O_1-H_{30} (2.07 Å). The molecular structure of KB was further confirmed by the ORTEP diagram obtained from single-crystal X-ray diffraction. The ORTEP representation with thermal ellipsoids at 50% probability is shown in Fig. 1. Together with lengthy O-H and O-C contacts, these distortions demonstrate how intramolecular hydrogen bonding stabilizes the whole structure. The calculated bond lengths, bond angles, and hydrogen bonding interactions provide the foundation for all subsequent spectroscopic and electronic analyses which establishes the reliability of the molecule.

4.2. UV–Visible and DOS spectral analysis

The TD-DFT/B3LYP approach determines the high absorption (λ max) of KB using a 6–311++G (d,p) basis set. Table 2 summarizes the UV–visible spectrum properties, including excitation energy, main and minor contributions of electronic transitions, oscillator strength (f), and (λ max) absorption. This prominent absorption band is primarily caused by the electron transition from HOMO to LUMO [16]. Three distinct

Table 1
Bond length (Å) and Bond angle (Degree) of KB compound.

Bond length (Å)	B3LYP/ 6-311++G (d, p)	Bond length (Å)	B3LYP/ 6-311++G (d, p)	Bond Angle (°)	B3LYP/6-311++G (d, p)
O_1-C_2	1.42	C_{11}-H_{32}	1.09	C_2-O_1-C_{11}	148.52
O_1-C_9	1.42	C_{11}-H_{33}	1.09	C_2-O_1-O_{12}	165.30
O_1-C_{11}	2.35	O_{12}-H_{34}	0.96	C_9-O_1-O_{12}	57.17
O_1-O_{12}	2.82	C_{13}-C_{14}	1.53	C_{11}-O_1-H_{30}	133.11
O_1-H_{30}	2.07	C_{13}-O_{21}	1.42	O_{12}-O_1-H_{30}	135.63
C_2-C_3	1.53	C_{13}-H_{35}	1.09	O_6-C_5-H_{26}	110.86
C_2-C_9	2.38	C_{14}-O_{15}	1.41	C_7-C_5-H_{26}	109.13
C_2-H_{24}	1.09	C_{14}-C_{16}	1.52	C_5-O_6-H_{27}	105.83
C_2-H_{30}	1.09	C_{14}-H_{36}	1.10	C_5-C_7-O_8	107.04
C_3-O_4	1.42	O_{15}-H_{37}	0.96	C_5-C_7-C_9	111.46
C_3-C_5	1.54	C_{16}-O_{17}	1.42	C_5-C_7-H_{28}	108.30
C_3-H_{25}	1.09	C_{16}-C_{18}	1.52	O_8-C_7-C_9	113.43
O_4-C_{13}	1.40	C_{16}-H_{38}	1.09	O_8-C_7-H_{28}	109.50
O_4-H_{42}	2.55	O_{17}-H_{39}	0.96	C_9-C_7-H_{28}	106.99
C_5-O_6	1.41	C_{18}-O_{19}	1.42	C_7-O_8-H_{29}	107.49
C_5-C_7	1.52	C_{18}-C_{20}	1.54	O_1-C_9-C_7	110.26
C_5-H_{26}	1.09	C_{18}-H_{40}	1.10	O_1-C_9-O_{10}	111.8204
O_6-H_{27}	0.96	O_{19}-H_{41}	0.97	C_2-C_9-C_7	82.80
C_7-O_8	1.42	C_{20}-O_{21}	1.43	C_2-C_9-O_{10}	103.60
C_7-C_9	1.54	C_{20}-C_{22}	1.52	C_2-C_9-C_{11}	136.01
C_7-H_{28}	1.09	C_{20}-H_{42}	1.09	C_7-C_9-O_{10}	105.83
O_8-H_{29}	0.96	C_{22}-O_{23}	1.43	C_7-C_9-C_{11}	114.20
C_9-O_{10}	1.40	C_{22}-H_{43}	1.09	C_7-C_9-H_{30}	80.13
C_9-C_{11}	1.53	C_{22}-H_{44}	1.09	O_{10}-C_9-C_{11}	109.28
C_9-H_{30}	2.60	O_{23}-H_{45}	0.96	O_{10}-C_9-H_{30}	80.52
O_{10}-H_{31}	0.97			C_{11}-C_9-H_{30}	158.10
C_{11}-O_{12}	1.42			C_9-O_{10}-H_{31}	104.95

Bond Angle (°)	B3LYP/ 6-311++G (d, p)	Bond Angle (°)	B3LYP/ 6-311++G (d, p)	Bond Angle (°)	B3LYP/ 6-311++G (d, p)
O_1-C_{11}-H_{32}	85.04	C_{14}-C_{13}-H_{35}	111.05	C_{18}-C_{16}-H_{38}	108.34
O_1-C_{11}-H_{33}	143.18	O_{21}-C_{13}-H_{35}	104.98	C_{16}-O_{17}-H_{39}	106.18
C_9-C_{11}-O_{12}	106.31	C_{13}-C_{14}-O_{15}	109.35	C_{16}-C_{18}-O_{19}	106.69
C_9-C_{11}-H_{32}	109.61	C_{13}-C_{14}-C_{16}	109.59	O_1-C_2-C_3	111.25
C_9-C_{11}-H_{33}	108.80	C_{13}-C_{14}-H_{36}	106.84	O_1-C_2-H_{24}	106.84
O_{12}-C_{11}-H_{32}	111.58	O_{15}-C_{14}-C_{16}	111.95	C_3-C_2-C_9	97.61
O_{12}-C_{11}-H_{33}	111.54	O_{15}-C_{14}-H_{36}	110.75	C_3-C_2-H_{24}	109.19

Table 1 (*continued*)

Bond Angle (°)	B3LYP/ 6-311++G (d, p)	Bond Angle (°)	B3LYP/ 6-311++G (d, p)	Bond Angle (°)	B3LYP/ 6-311++G (d, p)
H_{32}-C_{11}-H_{33}	108.90	C_{16}-C_{14}-H_{36}	108.1	C_{16}-C_{18}-C_{20}	109.66
O_1-O_{12}-H_{34}	159.41	C_{14}-O_{15}-H_{37}	105.55	C_{16}-C_{18}-H_{40}	108.26
C_{11}-O_{12}-H_{34}	108.37	C_{14}-C_{16}-O_{17}	107.23	O_{19}-C_{18}-C_{20}	112.67
O_4-C_{13}-C_{14}	109.08	C_{14}-C_{16}-C_{18}	110.35	O_{19}-C_{18}-H_{40}	110.92
O_4-C_{13}-O_{21}	111.42	C_{14}-C_{16}-H_{38}	108.73	C_{20}-C_{18}-H_{40}	108.51
O_4-C_{13}-H_{35}	110.93	O_{17}-C_{16}-C_{18}	111.77	C_{18}-O_{19}-H_{41}	106.46
C_{14}-C_{13}-O_{21}	109.30	O_{17}-C_{16}-H_{38}	110.35	C_{18}-C_{20}-O_{21}	110.91
C_{18}-C_{20}-C_{22}	112.86	C_2-C_3-C_5	109.80	C_{20}-C_{22}-O_{23}	108.25
C_{18}-C_{20}-H_{42}	108.42	C_2-C_3-H_{25}	109.65	C_{20}-C_{22}-H_{43}	108.61
C_2-C_3-O_4	107.15	O_4-C_3-C_5	113.36	C_{20}-C_{22}-H_{44}	109.34
O_{21}-C_{20}-C_{22}	104.44	O_4-C_3-H_{25}	109.19	O_{23}-C_{22}-H_{43}	111.29
O_{21}-C_{20}-H_{42}	110.41	C_5-C_3-H_{25}	107.64	O_{23}-C_{22}-H_{44}	111.19
C_{22}-C_{20}-H_{42}	109.74	C_3-O_4-C_{13}	117.01	H_{43}-C_{22}-H_{44}	108.09
C_{13}-O_{21}-C_{20}	114.47	C_3-C_5-O_6	108.80	C_{22}-O_{23}-H_{45}	108.51
C_3-C_5-H_{26}	108.10	C_3-C_5-C_7	109.74	O_6-C_5-C_7	110.15

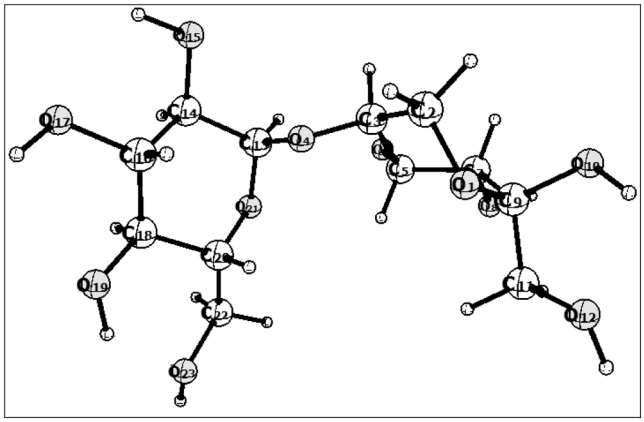

Fig. 1. Optimized ORTEP molecular structures of KB Compound.

absorption bands were detected in the gas phase at 372.76 nm, 314.34 nm, and 228.27 nm. These bands corresponded to excitation energies of 3.33 eV, 3.95 eV, and 4.30 eV respectively. A strong HOMO → LUMO transition (96%) is the main cause of the first transition at 372.76 nm, which has an oscillator strength of 0.0178 and indicates a π → π* excitation. The HOMO → L+2 transition accounts for 92% of the second band at 314.34 nm, with an oscillator strength of 0.0033. The HOMO → LUMO and HOMO → L+3 contribute just 3% and 3%, respectively. The HOMO → L+3 transition accounts for 95% of the third absorption at 228.27 nm, with a minor contribution from HOMO → L+2 (3%). The oscillator intensity of this absorption is 0.0159. These transitions validate the existence of permitted π → π* excitations, which are indicative of potential photophysical behaviour and suggest possible relevance in the development of bioactive or optoelectronic systems. Clear absorption maxima (λ-max) in the experimental UV-Vis spectrum allow for a reliable comparison of the electronic transitions predicted by TD-DFT.

Table 2
UV- Vis Absorption Wavelength (λmax) on KB.

Solvent state	Absorption band λ max (nm)	Excitation Energy (eV)	Oscillation Strength (f)	Major Contributions Energy (%)	Minor Contributions Energy (%)
Gas	372.76	3.33	0.0178	HOMO->LUMO (π→π*) (96%)	HOMO->L+2 (π→π*) (3%)
	314.34	3.94	0.0033	HOMO->L+2 (π→π*) (92%) HOMO->LUMO (π→π*) 3%	HOMO->L+3 (π→π*) (3%)
	228.27	4.30	0.0159	HOMO->L+3 (π→π*) (95%)	HOMO->L+2 (π→π*) (3%)
Experiment	200				

This agreement backs up that the experimental results and the theoretical result are in line with each other [17]. The differences observed between the experimental absorption wavelengths and those derived from TD-DFT calculations arise from the use of gas-phase approximations and the inherent limitations of the chosen functional and basis set in the theoretical analyses. The experimental spectra, on the other hand, are influenced by interactions with the solvent, variations in temperature and the presence of intermolecular forces. The TD-DFT studies have demonstrated that such differences occur frequently, leading to qualitative comparison [18,19]. The result, which pulls information from the Gaussian log file, was examined and plotted as a graph using the Gauss Sum 3.0 tool to get the total density of the state (DOS) curve of the KB molecule. Chemical bonding, the molecule's energy gap, and the occupied and virtual molecular orbitals are the primary goals of DOS plots. The DOS spectrum uses unique colour coding to show the orbitals' energy distribution: green denotes the positive part (virtual orbitals) and red denotes the negative part (occupied orbitals). The energy gap is a key factor in influencing the electrical and optical properties of a molecule. It is visually represented in Fig. 2a and 2b by the separation between the lowest unoccupied molecular orbital (LUMO) and the highest occupied molecular orbital (HOMO). This investigation helps determine the stability and reactivity of the KB compound as well as the type of electronic transitions within the molecule. According to the orbital energy distribution in the DOS plot, HOMO–LUMO excitations are the main cause of substantial transitions, which is in agreement with the results of UV–visible spectral analysis.

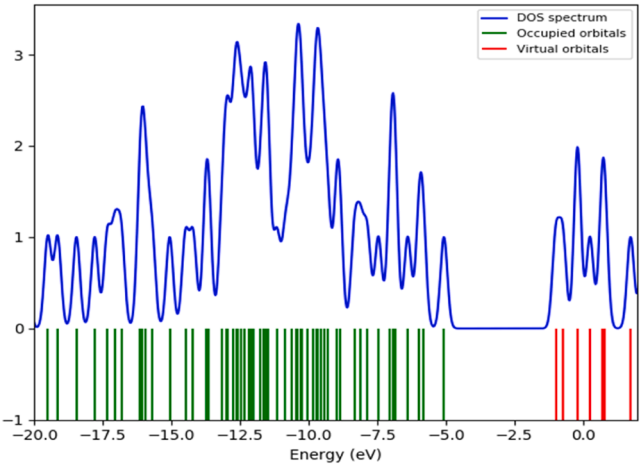

Fig. 2b. DOS spectrum of KB.

4.3. FT-IR spectrum

The theoretically simulated spectrum obtained at the B3LYP/6-311++G(d,p) level of theory was compared with the experimental FT-IR spectrum of the KB compound, which was recorded in the 4000–400 cm^{-1} range [20]. There are 45 atoms in the molecule KB ($C_{12}H_{22}O_{11}$). Since the molecule is non-linear, its 129 models can be divided into three primary categories according to the kind of atomic motion: torsional or wagging vibrations, bending, and stretching. In Fig. 3. and Table 3 show the most noticeable vibrations are stretching vibrations, which include motions of C–H, O–H, C–O, and C–C bonds and involve changes in bond lengths [21]. There are roughly 55 stretching modes in KB. Roughly 35 modes are contributed by bending vibrations, which include changes in bond angles like H–C–H, O–H, and C–O–C angles. The remaining 39 modes are torsional or wagging vibrations, which include out-of-plane motions, twisting, or rocking of groups like the sugar ring structure, OH, and CH_2. Although precise assignments for each mode necessitate computational analysis using techniques like DFT/B3LYP, these classifications offer a framework for comprehending the vibrational behavior of the molecule [22]. To account for anharmonicity and limitations in the basis set, the theoretical vibrational frequencies were scaled by a factor of 0.96. This resulted in a very good agreement with the absorption bands that were observed in the experiment. Sacrose, or

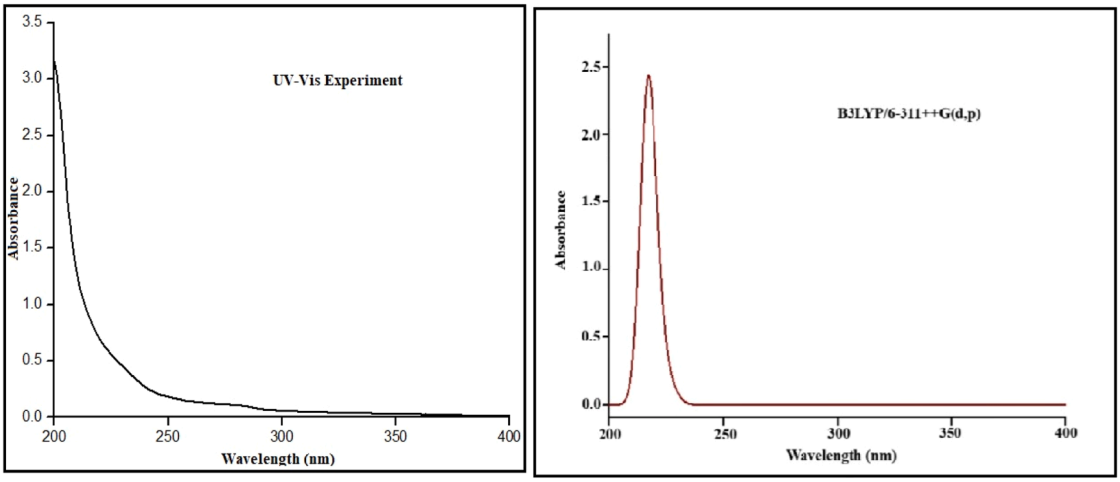

Fig. 2a. UV–Visible of KB.

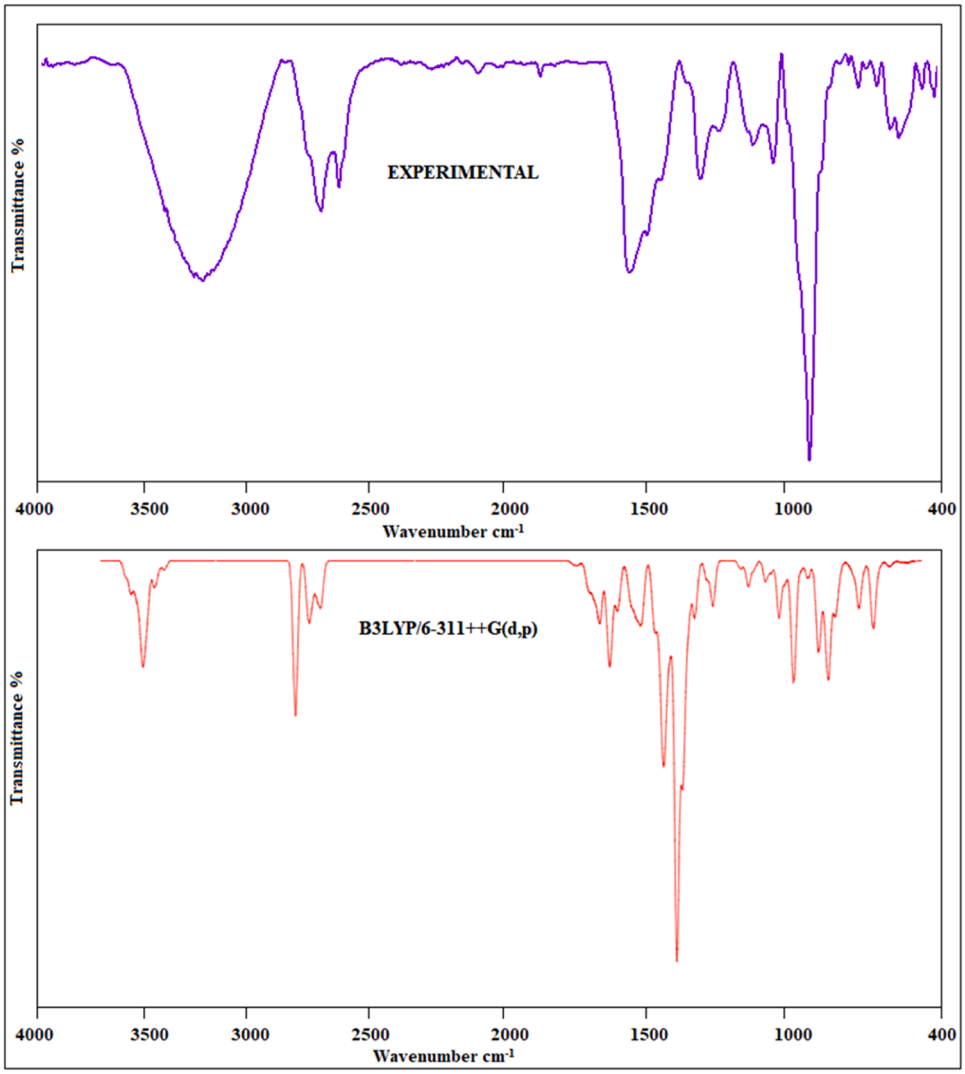

Fig. 3. FT-IR spectrum of KB molecules.

$C_{12}H_{22}O_{11}$, is a non-reducing disaccharide because it lacks a free carbonyl group but has several hydroxyl groups and a glycosidic ether bond.

The presence of extensive C–O and C–O–C bonding, characteristic of sugar molecules, is confirmed by its FT-IR spectrum, which is mainly characterized by a strong, broad O–H stretch around 3600–3200 cm^{-1}, aliphatic C–H stretches near 3000–2850 cm^{-1}, and intense C–O stretching bands in the 1150–1000 cm^{-1} region [23]. The presence of non-hydrogen-bonded hydroxyl groups in the molecular structure is indicated by a sequence of strong, sharp bands seen in the high wavenumber region 3690–3580 cm^{-1}. These bands correspond to free O–H stretching vibrations. Medium-to-strong intensity bands in the 3015–2850 cm^{-1} range, originating from both aromatic and aliphatic C–H moieties, confirmed the C–H stretching vibrations. In the 1475–1350 cm^{-1} range, the aromatic ring deformation and H–C–H bending vibrations are clearly visible and exhibit good agreement with the calculated deformation modes. The compound's most distinctive spectral feature is the strong C–O stretching band, which is visible in the 1120–1065 cm^{-1} range and is in good agreement with the high PED contribution that was theoretically predicted [24]. The 1028–750 cm^{-1} region exhibits additional Skeletal and fingerprint vibrations, primarily as a result of C–O and C–C stretching and in-plane bending. Additionally, below 625 cm^{-1}, torsional and out-of-plane deformation modes emerge, which correspond to the τHOCC, τHCOC, and ring-wagging motions that the computational model predicted. The FT-IR spectrum shows aliphatic CH_2/CH_3 stretches at 3034–2991 cm^{-1} (PED ≈ 48%), mixed aromatic/unsaturated C–H stretches at 3114–3047 cm^{-1} (PED ≈ 48%), and aromatic C–H stretching at 3141/3140 cm^{-1} (PED 92%). These FT-IR spectra confirm the presence of both aromatic and aliphatic frameworks in the molecule, supporting its structural rigidity and functional group orientation. The overall close correlation between the experimental spectrum and the vibrational frequencies and their mode assignments obtained by DFT validates the stability and structural integrity of the optimized geometry of KB.

4.4. NMR analysis

The chemical shifts of KB were predicted by DFT calculations through the GIAO technique is used to predict the theoretical chemical shifts for ^{1}H and ^{13}C from B3LYP/6–311++G (d,p).and their strong agreement with experimental NMR data validates the method's structure and dependability. The experimental NMR data of Table 4 and Fig. 4. Displayed in the supplied Bruker spectrum was compared to the theoretical values [25,26]. The ^{1}H and ^{13}C NMR spectra were recorded in D_2O (deuterium oxide) as the solvent. Several distinct peaks that are characteristic of carbohydrate protons can be seen in the ^{1}H NMR spectrum, which was recorded in the range of roughly 3.3 to 5.5 ppm. The ring protons and hydroxyl-bearing methine groups of the glucose units are represented by the high-resolution peaks between 3.3 and 4.0

Table 3
Experimental and theoretical FT-IR vibrational frequencies of KB.

Calculated frequency (cm^{-1})	Experimental FT-IR (cm^{-1})	Vibrational Assignments + (PED %)	Calculated frequency (cm^{-1})	Experimental FT-IR (cm^{-1})	Vibrational Assignments + (PED %)
3847	3750	υOH (100)	1375	1350	δHOC (11)
3839	3800	υOH (100)	1365	1350	δHCO (63)
3824	3800	υOH (100)	1339	1330	δHOC (19)
3803	3800	υOH (100)	1323	1300	δHCO (44)
3790	3800	υOH (100)	1292	1300	δHCO (55)
3784	3750	υOH (100)	1259	1250	δHOC (11)
3730	3750	υOH (100)	1244	1250	υCC (10)
3728	3750	υOH (100)	1240	1400	δHCO (26)
3141	3140	υCH (92)	1168	1150	υOC (13) +(24)
3114	3100	υCH(48)	1139	1120	υOC (13)
3096	3100	υCH(48)	1123	1120	υOC (26)
3047	3050	υCH(48)	1117	1100	υCC (16)+ τHCOC (10)+ δHOC (14)
3034	3000	υCH (48)	987	1000	υOC (29)
3034	3050	υCH (48)	938	900	υCC (15)
2991	3000	υCH (48	913	900	υCC (10)
1522	1530	τHCCC (18) + δHCH (72)	786	780	υCC (19)
1538	1530	δHCH (85)	650	650	δOCO (24)
1508	1500	δHCH (82)	615	600	τHOCC (25)+ OUT OCOC(16)
1477	1450	δHOC (24)	588	585	δOCO (10)
1467	1450	τHCCC (20)	588	585	δOCC (10)
1452	1450	δHCO (16)	410	400	δOCC (12)
1446	1450	OUT CCCH (16)	450	450	δCCO (16)
1424	1420	OUT CCCH (10)	489	500	δCCO (10)
1416	1400	δHOC (43)	439	450	τHOCC (68)
1392	1400	τHCOC (15)	406	400	τHOCC (65)

Table 4
Theoretical NMR chemical shift values of KB.

Atom	Theoretical Chemical Shift in ppm	Experimental chemical shift in ppm	Atom	Theoretical Chemical Shift in ppm	Experimental chemical shift in ppm
C13	63.43	60.68	H24	26.99	3.63
C7	67.65	69.64	H44	27.18	3.71
C3	70.60	70.04	H38	27.44	3.75
C16	71.21	71.54	H28	27.70	3.76
C18	71.17	71.71	H25	27.83	3.79
C14	72.06	72.68	H43	27.78	3.80
C20	74.00	74.35	H36	27.90	3.82
C5	75.01	75.75	H33	27.99	3.84
C22	78.68	78.39	H31	28.21	3.87
C11	82.64	89.34	H40	28.71	3.92
C9	95.14	96.19	H39	31.14	3.94
C2	94.49	97.62	H37	31.33	4.80
H30	2.72	3.46	H41	31.45	5.08
H32	2.99	3.53	H34	31.84	5.09
H35	2.86	3.54	H27	32.06	5.38
H42	2.22	3.55	H29	32.16	5.42
H26	2.67	3.61	H45	32.85	5.43

ppm. Interestingly, downfield signals at 5.08, 5.09, 5.38, and 5.43 ppm are indicative of anomeric protons and protons next to glycosidic linkages, confirming the presence of α (1→2) glycosidic bonds that are typical of KB [27–28]. Theoretical values like H37 (4.80 ppm vs. 3.94 ppm exp.), H41 (5.08 ppm vs. 5.08 ppm), and H45 (5.43 ppm vs. 5.43 ppm) show exceptionally high accuracy for the 1H NMR spectrum, indicating accurate modeling of hydrogen bonding and ring conformations. The majority of protons in the sugar ring are found in the 3.4–4.0 ppm range, and computed shifts (such as H30 at 2.72 ppm versus 3.46 ppm) typically represent accurate electronic environments. As is common for sugars, carbon resonances in the ^{13}C NMR spectrum range from 60 to about 100 ppm. Because the glycosidic carbons are not shielded, the anomeric carbons show up at 97.62 ppm (C2) and 96.19 ppm (C9). 89.34 ppm (C11) and 78.39–60.68 ppm for the ring and side-chain carbons are two additional noteworthy peaks. These chemical shifts validate the β-D-glucopyranosyl-(1→2)-D-glucose linkage and are in agreement with pyranose ring structures. Key carbon atoms like C2 (94.49 ppm theoretical vs. 97.62 ppm experimental), C9 (95.14 vs. 96.19 ppm), and C11 (82.64 vs. 89.34 ppm) have calculated chemical shifts in the 13C NMR spectrum that show good correlation, with minor deviations probably caused by solvent effects, temperature, and the theoretical model's limitations. The anticancer relevance of KB was supported by the confirmation of α (1→2) glycosidic linkage, the presence of multiple hydroxyl groups in the protein, which suggests a strong hydrogen bonding potential, and the distinct downfield shifts of the anomeric protons (5.08–5.43 ppm) and carbons (96–97 ppm), which indicate electron-deficient environments and potential interactions with cancer-related targets. Using distinct chemical shift patterns for both the proton and carbon nuclei, the NMR data show a pure sample with well-defined linkage patterns, which confirms KB's structure, conformation, and stereochemistry.

4.5. Frontier molecular orbital

Frontier molecular orbitals, which include the highest occupied molecular orbital (HOMO) and the lowest unoccupied molecular orbital (LUMO), are crucial for comprehending the most reactive locations in conjugated systems as well as molecular stability and charge transport inside molecules [29]. Moderately high energy molecules can easily participate in oxidation or nucleophilic reactions and are frequently useful electron donors [30]. The KB compound's energy gap (ΔE) and HOMO-LUMO visualization are shown in Fig. 5. When determining the molecules' chemical reactivity, the energy gap is a crucial factor. It offers details on the phenomenon of charge transfer as well. A variety of quantum chemical factors are also suggested by the HOMO-LUMO energies [31]. When the HOMO-LUMO energy gap widens, a molecule's polarizability, electron mobility, and adaptability all decrease [32]. The FMO parameters—such as the complexes' electrophilicity index, chemical hardness, chemical softness, and electronegativity—that were calculated using energy gap values are listed in Table 5.The KB compound has a HOMO–LUMO energy gap (ΔE) of –8.02 eV due to its reported HOMO energy (EHOMO) of 6.78 eV and LUMO energy (ELUMO) of –1.24 eV. The molecule's low reactivity and great chemical stability are indicated by this significant negative energy difference. The compound's donor-acceptor behaviour is reflected in the electron affinity

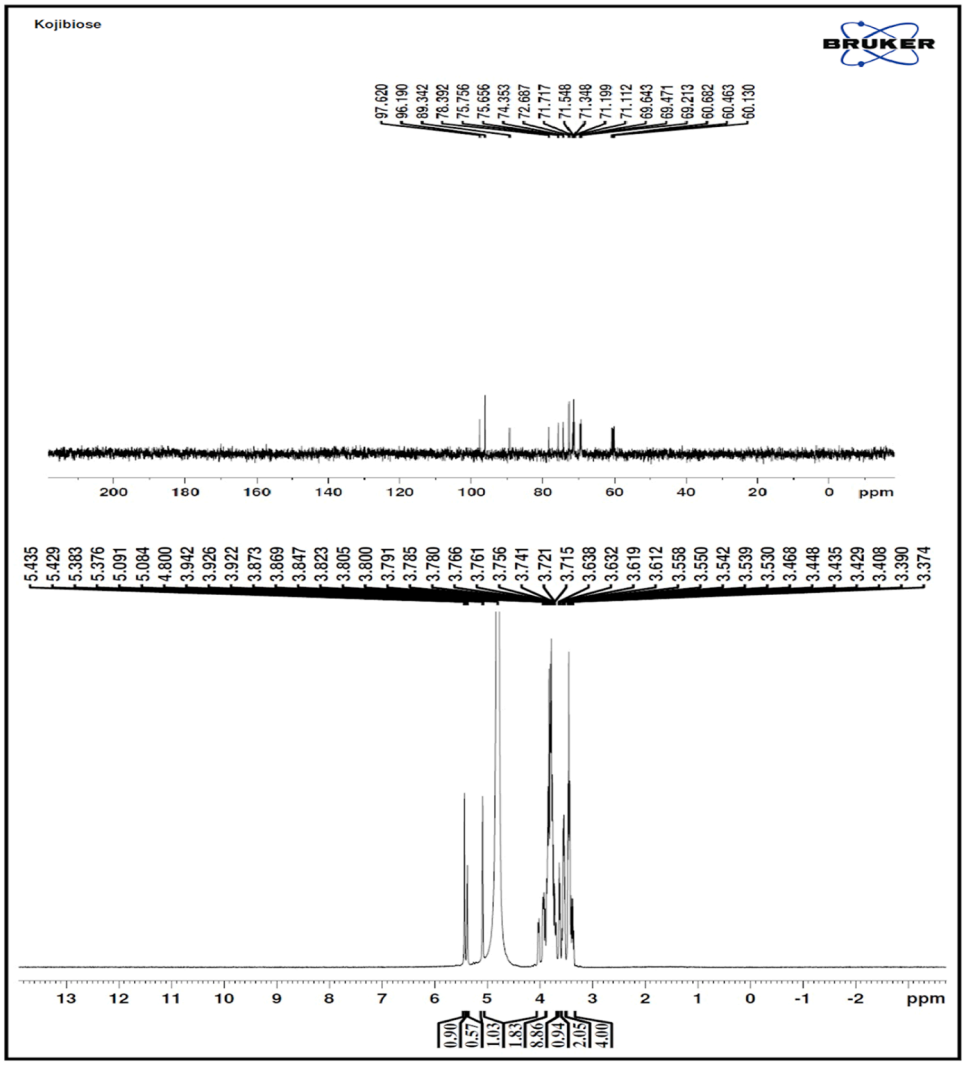

Fig. 4. Chemical shift KB with 1H and 13C.

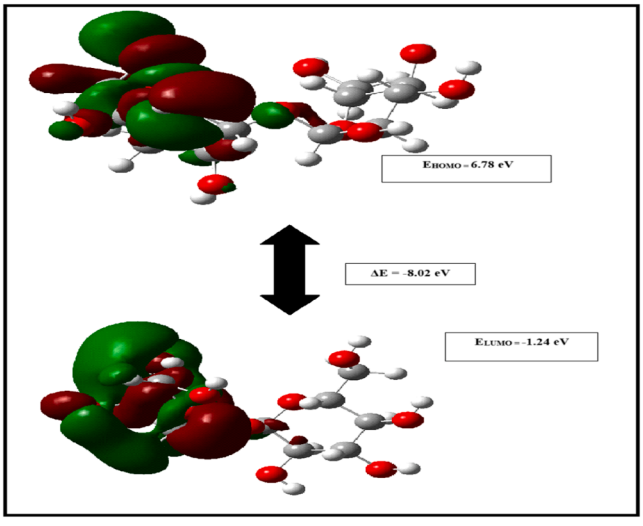

Fig. 5. E_{HOMO}, E_{LUMO}, and energy Gap of KB molecules.

(EA), which is 1.24 eV, and the ionization potential (IP), which is determined by subtracting the HOMO energy. A balanced distribution of

Table 5
Chemical stability & reactivity on KB molecules.

Electronic Properties	Values eV	Electronic Properties	Values eV
E_{HOMO} (eV)	-6.78 eV	Chemical hardness (η)	-4.01 eV
E_{LUMO} (eV)	1.24 eV	Chemical softness (σ)	-0.12eV^{-1}
EHOMO–ELUMO (eV)	-8.02 eV	Electrophilicity Index (ω)	-0.96eV
Ionization potential (IP)	-6.78 eV	Nucleophilicity Index 1/	-1.04 eV^{-1}
Electron affinity (EA)	1.24 eV	Electron donor power (ω^-)	0.15 eV
Electronegativity(χ)	-2.77eV	Electron acceptor power (ω^+)	-0.07 eV
Chemical potential (μ)	2.77eV	ΔNmax (eV)	-0.69 eV

electron density is shown by the predicted chemical potential (μ) and electronegativity (χ), which are 2.77 eV and –2.77 eV, respectively. The molecule's resistance to charge deformation is demonstrated by its chemical softness (σ) of -0.12 eV^{-1} and chemical hardness (η) of -4.01 eV. The KB compound appears to be more likely to donate electrons than to accept them, as indicated by the electrophilicity index (ω) of -0.96 eV and the nucleophilicity index of -1.04 eV^{-1}. It also supports its greater donor features with calculated electron donor power (ω^-) of 0.15 eV and electron acceptor power (ω^+) of -0.07 eV. With a maximal electronic charge transfer (ΔN_max) of -0.69 eV, it can interact with an electrophilic or nucleophilic environment with a moderate ability to transfer charges. HOMO–LUMO analysis provides insight into the chemical stability, reactivity, and electron donor–acceptor behaviour of KB. The

energy gap helps to explain its low reactivity, potential biological and electronic applications of the molecule

4.6. Mulliken charge distribution

Mulliken charge analysis is a widely used technique for evaluating a molecule's chemical and physical properties. Mulliken charges are used to detect electrophilic and nucleophilic regions by determining the structure's positive and negative charge density regions. Understanding how the molecule might interact with other chemical species or biological targets requires knowledge of this information [33–35]. Mulliken charge analysis, calculated at the B3LYP/6-311++G(d,p) level of theory, was carried out for the KB molecule in the current work. With this method, the electron distribution across the molecule structure may be thoroughly examined, and possible locations for reactivity and intermolecular interaction can be assessed. The distribution of Mulliken charges for compound KB is seen in Table 6. The findings show that the oxygen atoms (O_4, O_6, O_8, O_{10}, O_{12}, O_{15}, O_{17}, O_{19}, O_{21}, and O_{23}) have noticeably negative charges between –0.44 and –0.57 eV, which is indicative of their strong electron-withdrawing nature and high electronegativity. It is probable that these atoms will function as potent nucleophilic sites, able to participate in electrostatic interactions such as hydrogen bonding. In terms of nucleophilic potential, O_{17} appears to be the most reactive oxygen site among them due to its largest negative charge (-0.57 eV).A number of hydrogen atoms, however, have significant positive charges (H_{27} = 0.31 eV, H_{29} = 0.31 eV, H_{31} = 0.32 eV, H_{37} = 0.32 eV, and H_{39} = 0.32 eV), which suggests that they participate in strong hydrogen bonding interactions with electron-rich sites. To further strengthen their electropositive nature, these hydrogen atoms are usually bound to electronegative oxygen atoms. Different levels of charge were displayed by the carbon atoms in the structure: C_{13} had the most positive charge (0.34 eV), while C_2 had the lowest charge (–0.24 eV). This variability may affect the chemical reactivity of KB by emphasizing localized electronic environments within its molecular framework, especially in biological interactions or docking with active sites.

4.7. NBO analysis

In molecular systems, the NBO analysis is a beneficial technique for elucidating intramolecular and intermolecular bondings as well as interactions between bonds. The analysis of charge transfers or hyperconjugation interactions inside the molecules is also made easier show in Fig. 6. The degree of conjugation throughout the system is facilitated by the interactions between electron donors and electron acceptors intensifying when the stabilizing energy $E^{(2)}$ associated with electron delocalization between donor and acceptor in the NBO analysis is significant [36,37].In accordance with the findings of the NBO analysis, the system's standard orientation is specified in the Gaussian output file. The

Table 6
Mulliken charges of the compound KB.

Atoms	Charges (eV)	Atoms	Charges (eV)	Atoms	Charges (eV)
O_1	-0.07	C_{16}	0.138408	H_{31}	0.34
C_2	-0.24	O_{17}	-0.56913	H_{32}	0.09
C_3	0.11	C_{18}	0.128424	H_{33}	0.04
O_4	-0.51	O_{19}	-0.55572	H_{34}	0.13
C_5	0.10	C_{20}	0.161816	H_{35}	0.14
O_6	-0.54	O_{21}	-0.51612	H_{36}	0.09
C_7	0.19	C_{22}	0.011316	H_{37}	0.34
O_8	-0.52	O_{23}	-0.52219	H_{38}	0.11
C_9	0.27	H_{24}	0.072414	H_{39}	0.34
O_{10}	-0.52	H_{25}	0.125452	H_{40}	0.08
C_{11}	0.03	H_{26}	0.140955	H_{41}	0.31
O_{12}	-0.44	H_{27}	0.307535	H_{42}	0.17
C_{13}	0.34	H_{28}	0.109387	H_{43}	0.05
C_{14}	0.19	H_{29}	0.312361	H_{44}	0.10
O_{15}	-0.55	H_{30}	0.27714	H_{45}	0.30

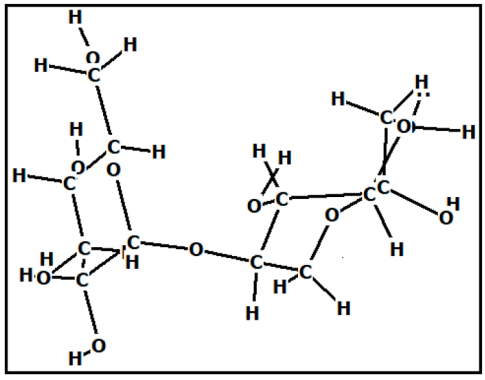

Fig. 6. Intra- and intermolecular hydrogen bonding of KB.

delocalization stabilization energy $E^{(2)}$ is computed for each donor NBO (i) and acceptor NBO (j). The KB molecule's NBO analysis is carried out using the DFT/B3LYP/6-311++G(d,p) method [38]. In Table 7, a number of NBO values are displayed. Stabilization energy $E^{(2)}$ was used to study the transitions of electron interactions between donors and acceptors, indicating strong interactions. With a very high stabilization energy $E^{(2)}$ = 137.88 kcal/mol, the highest hyperconjugative interaction is seen between the bonding orbital of O_1–C_2 (σ) and the antibonding orbital C_2–H_{30} (σ*), suggesting considerable charge delocalization. Additionally, O_1–C_2 (σ*) and O_1–C_9 (σ*), which have comparable $E^{(2)}$ values of 67.71 and 31.58 kcal/mol, respectively, get electron donations from the C_2–H_{30} (σ) orbital. These interactions reinforce molecule stability by indicating a strong intramolecular donor–acceptor connection. Significant contributions are also made via lone pair (LP) interactions. In order to stabilize the structure, lone pair–bond interactions are crucial. The LP (2) of O_{12} donates to O_1–C_2 (σ*) with an $E^{(2)}$ value of 17.17

Table 7
Fock matrix analysis using second order perturbation theory in NBO.

Donor (i)	Type	Acceptor (j)	Type	$E^{(2)}$ (kcal/mol[1])	E (j)-E(i) (a. u.)	F (i, j) (a. u.)
O_1 - C_2	σ	O_1 - C_2	σ*	17.58	1.27	0.134
O_1 - C_2	σ	C_2 - H_{30}	σ*	137.88	2.38	0.514
O_1 - C_9	σ	C_2 - H_{30}	σ*	26.22	2.33	0.225
O_1 - C_9	σ	C_{11} - O_{12}	σ*	10.72	1.03	0.095
C_2 - C_3	σ	C_2 - H_{30}	σ*	25.5	2.21	0.219
C_2 - H_{24}	σ	C_2 - H_{30}	σ*	21.99	2.1	0.199
C_2 - H_{30}	σ	O_1 - C_2	σ*	67.71	1.32	0.273
C_2 - H_{30}	σ	O_1 - C_9	σ*	31.58	1	0.163
C_2 - H_{30}	σ	C_2 - H_{30}	σ*	20.48	2.43	0.203
C_2 - H_{30}	σ	C_9 - C_{11}	σ*	23.63	1.14	0.152
C_9 - C_{11}	σ	O_1 - C_2	σ*	9.85	1.07	0.095
C_{11} - O_{12}	σ	O_1 - C_2	σ*	23.15	1.32	0.161
O_1	LP (1)	O_1 - C_2	σ*	9.53	0.96	0.086
O_1	LP (1)	C_2 - C_3	σ*	9.62	0.88	0.084
O_1	LP (1)	O_{12} - H_{34}	σ*	14.06	0.96	0.104
O_1	LP (2)	O_1 - C_2	σ*	12.75	1.06	0.104
O_1	LP (2)	O_{12} - H_{34}	σ*	44.4	1.06	0.197
O_4	LP (2)	C_{13} - O_{21}	σ*	10.91	0.63	0.075
O_{10}	LP (2)	O_1 - C_9	σ*	21.39	0.62	0.105
O_{12}	LP (2)	O_1 - C_2	σ*	17.17	1.1	0.125
O_{12}	LP (2)	O_{12} - H_{34}	σ*	9.78	1.09	0.093
O_1 - C_2	σ*	C_2 - H_{30}	σ*	18.42	1.11	0.313
O_1 - C_9	σ*	C_9 - O_{10}	σ*	15.19	0.07	0.083

kcal/mol, while O_1 LP(2) → O_{12}–H_{34} (σ*) provides 44.40 kcal/mol. At 21.39 kcal/mol, O_{10} LP(2) → O_1–C_9 (σ*) also exhibits a significant stabilization. Additional significant interactions that show extensive delocalization throughout the molecule's bonding framework include C2–H24 (σ) → C2–H30 (σ*) ($E^{(2)} = 21.99$ kcal/mol), C_9–C_{11} (σ) → O_1–C_2 (σ*) ($E^{(2)} = 9.85$ kcal/mol^1), and C_{11}–O_{12} (σ) → O_1–C_2 (σ*) ($E^{(2)} = 23.15$ kcal/mol). Significant intramolecular charge delocalization is confirmed by the NBO analysis, supporting the overall conjugation, stability, and reactivity of the KB molecule. Additionally, it demonstrates strong donor-acceptor interactions via lone pair orbitals and bonding.

4.8. Topology parameters

The surface density of the electron pair can be estimated using the topological characteristics, such as LOL and ELF [39]. These are the areas of the molecular area that are most likely to contain each pair of electrons. Multiwfn 3.8 produced a contour map and color file projection map of ELF for the KB molecule, which are seen in Fig. 7a and 7b both bound and nonbonded local electron pairs are included in the electron pair density and scheme configuration, which is generally represented by ELF on a scale of 0 to 1.0. The supplied molecule's electron field is delocalized if the value is less than 0.2. The ELF map of the KB molecule clearly shows regions of high localization (ELF > 0.8) in regions that correspond to lone pairs and bonding electron pairs, particularly around electronegative elements like oxygen, which indicates strong covalent connections. On the other hand, delocalized electrons, which are frequently associated with π-conjugation or steric repulsion, are suggested by low ELF values (< 0.2) found in specific molecular areas. Likewise, LOL characterizes the majority of the localized orbital coverage, and the map surface falls between 0 and 1 [40,41]. High values in σ-bonding regions (LOL > 0.7) on the KB LOL map suggest localized orbital density, although relatively lower values in some extended molecular domains indicate partial delocalization. The distribution of localized and delocalized electron densities within the KB molecule is thus clearly shown by the ELF and LOL investigations. These results are consistent with the study's main goal, which is to investigate the KB compound's electrical structure and bonding characteristics. The structural stability, electrical configuration, and possible biological or pharmacological significance of the chemical are all supported by the information gleaned from ELF and LOL maps.

4.9. MEP analysis

A colour band is used by the Molecular Electrostatic Potential (MEP) surface to show how electrostatic potential is distributed throughout a molecule, which aids in locating reactive regions. Red < orange < yellow < green < blue are the possible increases in order. Whereas blue indicates locations that lack electrons (nucleophilic sites), green indicates neutral zones, and red indicates areas that are abundant in electrons (electrophilic sites). Understanding electrophilic and nucleophilic elements of chemical reactions, such as intramolecular charge transfer, hydrogen bonding, and other molecular interactions, requires the use of MEP analysis. It is possible to distinguish between areas vulnerable to electrophilic and nucleophilic attacks by mapping the electrostatic potential at different points on the molecular surface [42, 43].As can be seen in Fig. 8 the MEP map of the KB compound displays a consistent electrostatic potential pattern with distinct reactive site distinction. The oxygen atoms of the hydroxyl and glycosidic groups are the most negatively charged areas (red) in both maps, indicating that they are the primary electron-rich sites linked to strong hydrogen-bond acceptance and electrophilic attack. In order to identify the hydroxyl hydrogens and the anomeric carbon as electron-deficient centers that are vulnerable to nucleophilic attack and function as hydrogen-bond donors, positive areas (blue) are seen surrounding them. In contrast, the C–C and C–H bonds primarily show neutral to slightly positive potential (green to light blue), suggesting comparatively little reactivity in comparison to anomeric and oxygen-rich regions. These carbon bonds primarily support the molecule's steric profile and structural makeup. The worldwide distribution of the MEP surface is shown in Figure 7, whereas the localized reactive centers, including the relative neutrality of the carbon backbone, are more clearly distinguished in Fig. 8. When taken together, the two representations show that the carbon framework stabilizes the molecule conformation and supports hydrogen-bonding networks, while the polar oxygen functions of KB play a major role in determining its reactivity.

4.10. Antibacterial activity

The antibacterial activity of kojibiose was evaluated using the agar well diffusion method against *Escherichia coli* and *Staphylococcus aureus*. The results in Fig. 9. show the diameter of inhibition zones (mm). Kojibiose exhibited significant inhibition against *E. coli* with inhibition zones of 15 mm at 125 μg and 12 mm at 250 μg, while Streptomycin (positive control) produced a consistent inhibition zone of 23 mm. Similarly, for *S. aureus*, kojibiose displayed measurable activity, showing inhibition zones of 15 mm at 125 μg and 12 mm at 250 μg, compared to 23 mm for the standard antibiotic. The negative control (DMSO) showed no inhibitory effect, confirming the reliability and specificity of the assay. These findings demonstrate that kojibiose exhibits notable antibacterial activity against both *E. coli* and *S. aureus*. Although the inhibition zones were slightly smaller than those of Streptomycin, kojibiose still showed effective antibacterial potential warranting further exploration. The comparable activity against *E. coli* (Gram-negative) and *S. aureus* (Gram-positive) suggests that kojibiose

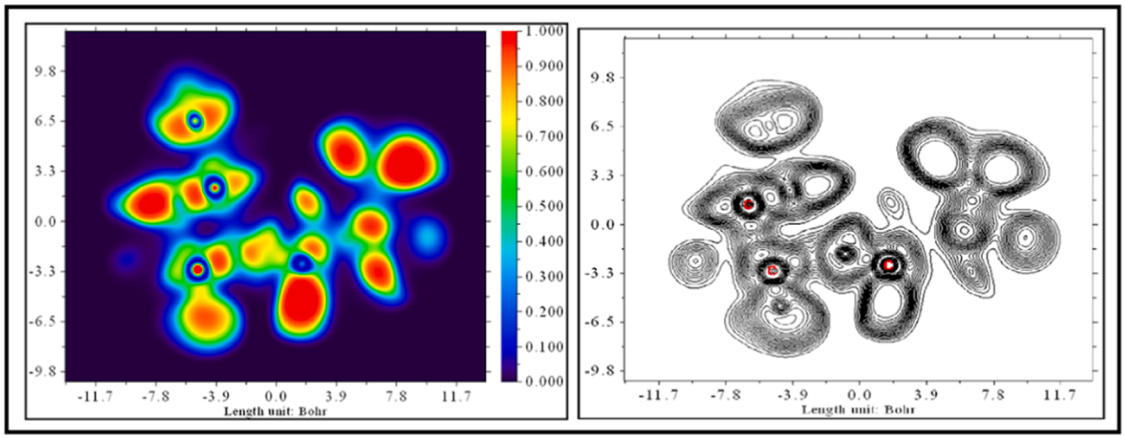

Fig. 7a. ELF (colour-filled map with contour-Line Map) on KB.

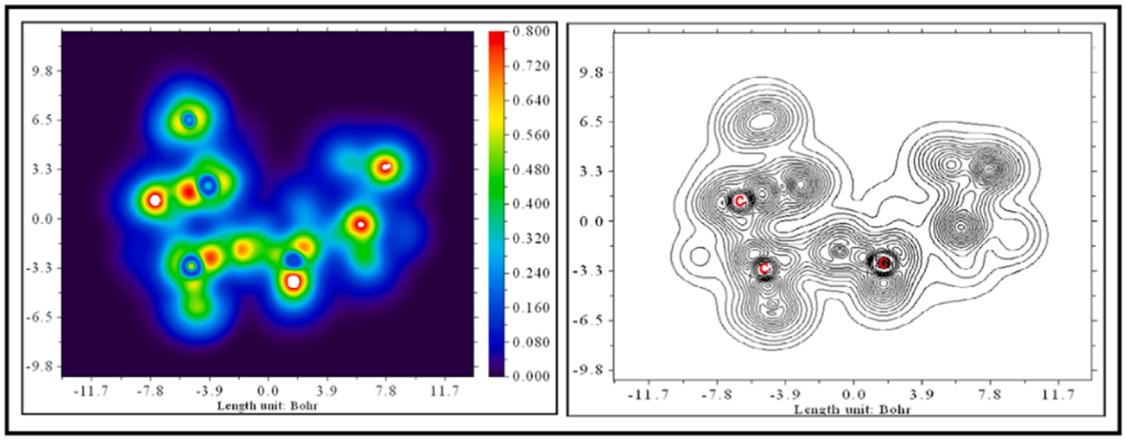

Fig. 7b. LOL (colour-filled map with contour-Line Map) on KB.

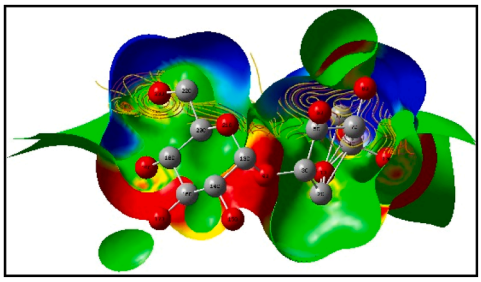

Fig. 8. MEP Map of KB Compound.

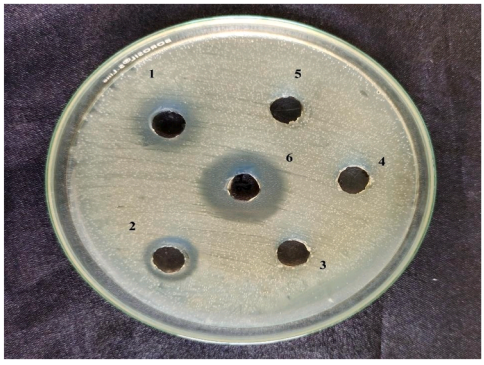

Fig. 9. Antibacterial activity of kojibiose against *E. coli* and *S. aureus*.

has a broad-spectrum antibacterial effect and can interact efficiently with different bacterial cell wall structures [44–47]. The presence of multiple hydroxyl groups in kojibiose may enhance its ability to form hydrogen bonds with bacterial cell components, contributing to its inhibitory action. Overall, these observations indicate that kojibiose, being a naturally derived disaccharide, could serve as a potential bioactive compound for antibacterial applications. Further studies involving minimum inhibitory concentration (MIC) determination and structure–activity relationship (SAR) analysis are recommended to elucidate its mechanism of action and therapeutic potential.

4.11. Nonlinear optical properties

The nonlinear optical properties were assessed at the B3LYP/6-311++G (d,p) level, with the results presented in table. The total dipole moment (μ_{total} = 5.71 D) indicates strong molecular polarity and efficient intramolecular charge transfer between donor and acceptor areas, which improves second-order NLO activity [48,49]. The isotropic polarizability (α = 159.26 a.u) and anisotropy (Δα = 32.35 a.u) show significant electronic delocalization and directional polarizability, indicating good molecule response to external electrical fields [50,51]. The first order hyperpolarizability (β_{total} = 251.93 a.u. = 2.18 × 10^{-30}esu) suggests a substantial second-order NLO response, dominated by β_x and β_y components, implying charge redistribution primarily inside the molecular plane. The second hyperpolarizability (γ = 1.57 × 10^5 a.u) enhances the molecule's ability to perform third-order optical operations like limiting and modulation. The calculated second order polarisability values are comparable in magnitude to those observed for other organic NLO-active molecules examined using similar DFT techniques. The current findings align with previously published work and reinforce the notion that the molecule is suitable for nonlinear optical application [52,53].

The Table 8 high *μ*, α, β and γ values indicate that the investigated molecule has significant nonlinear optical efficiency due to prolonged π-conjugation and strong intramolecular charge-transfer properties. The nonlinear optical property is complexly connected to the moderate HOMO-LUMO band gap of the molecule, facilitating charge movement between molecules and enabling electronic polarization to occur. This characteristic is frequently observed in organic NLO materials. The functional nonlinear optical property of this molecule arises from its oxygen-rich structure and uneven charge distribution, which promote effective intramolecular charge transfer and enhance electronic polarizability, leading to a significant first order hyperpolarizability as demonstrated by DFT calculations [54]. Strong molecule polarity and

Table 8
The calculated dipole moment (μ), polarizability (α), first-order hyperpolarizability (β), and second hyperpolarizability (γ) using B3LYP/6-311++G(d, p) level.

NLO Properties	DFT/ B3LYP	NLO Properties	DFT/B3LYP
(a) Dipole moment (μ) Debye		**(c) First-order Hyperpolarizability (β)**	
μ_x	3.2412	β_{xxx}	94.5239
μ_y	4.6333	β_{xxy}	78.6314
μ_z	2.2525	β_{xyy}	1.2748
μ_{total}	5.7146	β_{yyy}	98.6980
		β_{xzz}	−0.9769
(b) Polarizability		β_{yzz}	3.4924
α_{xx}	176.960	β_{zzz}	−0.3112
α_{yy}	159.519	β_{xyz}	−33.9085
α_{zz}	141.295	β_{total} (a.u.)	251.9282
<α>	159.2580 a.u.	β_{total} (e.s.u.)	2.18 × 10^{-30} esu
Δα	32.3500 a.u.	γ (a.u.)	1.57 × 10^5 a.u.

electronic flexibility are indicated by the computed total dipole moment of 5.71 Debye and mean polarizability of 159.26 a.u., which can encourage electrostatic interactions and hydrogen bonding with bacterial cell components. Additionally, improved intramolecular charge transfer is reflected in the unusually high first-order hyperpolarizability ($\beta = 2.18 \times 10^{-31}$ esu), which may facilitate interaction with bacterial membranes and hence assist the antibacterial activity.

4.12. Topological aspects

The optimized chemical structure of a molecule can be transformed into a molecular graph (G), where vertices represent atoms and edges represent bonds. In this graph, the degree $dG(i)$ of a vertex i denotes the number of edges incident to it, while the distance $dG(i,j)$ between any two vertices $\{i,j\}$ refers to the shortest path connecting them. The objective of this study is to apply the QSAR/QSPR approach using various degree-based topological descriptors to theoretically assess pharmacological activity. In chemical graph theory, molecular properties are inherently linked to structural features. This field enables the representation of molecules as graphs and facilitates the development of quantitative structure–property/activity relationship (QSPR/QSAR) models [55]. These models predict chemical behavior by correlating structural descriptors with physical, chemical, or biological properties. A typical QSAR/QSPR study involves three main steps: structure representation, descriptor calculation, and model development. Among various descriptors, topological indices provide a simple yet powerful means of converting structural information into numerical values that can be linked to molecular activity [56,57]. The topological indices used to predict the quantitative properties of the molecular structure, namely Kojibiose, contain the compound formula $C_{12}H_{22}O_{11}$ compound weight of 342.30 g/mol. Using various degrees-based topological indices such as Randic χ(G), Zagreb M1 (G) and M2 (G), Atom bond connectivity ABC (G), Sum connectivity SC (G), Geometric arithmetic GA (G), Harmonic H (G), third Zagreb ZG3 (G), Second Hyper-Zagreb HM2 (G), Forgotten F (G), and Symmetric division deg SSD (G). The above-mentioned degree-based topological indices are suitable for studying drug discovery that is used to prevent enormous biological activity. The KB molecules are analysed in this work utilising a range of degree-based topological markers through Fig. 10.

4.12.1. Definitions and mathematical aspects

Let G be the graph of KB, and E (i, j) denote the class of edges of G connecting vertices with degree i to degree j. From the neglected hydrogen of the KB chemical structure, observe the number of edges and the vertices that $|E_{1,2}| = 4$, $|E_{1,3}| = 2$, $|E_{2,2}| = 4$, $|E_{2,3}| = 6$, $|E_{2,4}| = 1$, $|E_{3,3}| = 4$ and $|E_{3,4}| = 3$

Definition 1. The Randic index is a well-established topological descriptor frequently applied in modeling chemical reactions and pharmacological properties, especially within QSAR and QSPR frameworks. It has been effectively utilized in the study of extremal trees associated with domination numbers [58]. Introduced by Randic, this index is defined on a graph G with a vertex set V(G) and edge set E(G), as described below:

$$x(G) = ij \in E(G)1didj$$

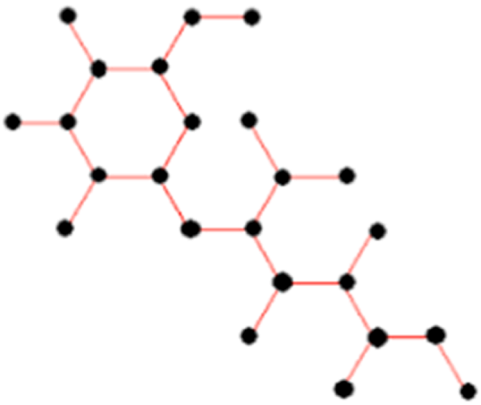

Fig. 10. Hydrogen depleted of KB compound.

[i] The result derived through the application of Definition 1 is outlined below:

$\chi(KB)=4 \times 11 \times 2+2 \times 11 \times 3+4 \times 12 \times 2+6 \times 12 \times 3+1 \times 12 \times 4+4 \times 13 \times 3+3 \times 13 \times 4$

$\chi(KB) = 2.8284 + 1.1547 + 2.0000 + 2.4494 + 0.3536 + 1.3332 + 0.8661 = 10.986$

Definition 2. The Zagreb indices were introduced nearly three decades ago by Gutman and Trinajestic [59]. These include the first and second Zagreb indices, which are defined as follows:

$$M1G = ij \in E(G)(di + dj)$$

and

$$M2(G) = ij \in E(G)didj$$

[ii] The result derived through the application of Definition 2 is outlined below:

M_1 (KB) $= 4 \times (1+2) +2 \times (1+3) + 4 \times (2+2) +6 \times (2+3) +1 \times (2+4) +4 \times (3+3) + 3 \times (3+4) = 117$

M_1 (KB) $= 117$

and

$M_2(KB) = 4 \times (1 \times 2) + 2 \times (1 \times 3) + 4 \times (2 \times 2) + 6 \times (2 \times 3) + 1 \times (2 \times 4) + 4 \times (3 \times 3) + 3 \times (3 \times 4)$

$M_2(KB) = 146$

Definition 3. The ABC index was established by Estrada et al. in 1998 and has been applied to the investigation of the strength of alkanes and strain energy of cycloalkanes [60]. The ABC index is defined as:

$$ABCG = ij \in E(G)di + dj - 2di \times dj$$

[iii] The result derived through the application of Definition 3 is outlined below:

$ABC(KB) = 43\text{-}21 \times 2+2 \times 4\text{-}21 \times 3+4 \times 4\text{-}22 \times 2+6 \times 5\text{-}22 \times 3+1 \times 6\text{-}22 \times 4+4 \times 6\text{-}23 \times 3+3 \times 7\text{-}23 \times 4$

$ABC(KB) = 4 \times 0.7071 + 2 \times 0.8165 + 4 \times 0.7071 + 6 \times 0.7071 + 4 \times 0.6667 + 3 \times 0.6455 = 16.843$

Definition 4. The increasing relevance of the connectivity index has led to the development of several variants, as documented in the literature. Among them, the sum-connectivity index (SC) and the atom-bond connectivity (ABC) index have gained considerable attention, particularly for their effectiveness in biological activity prediction. The ABC index was formulated based on the foundational principles of the SC index [61]. A newly introduced variation of the SC index is defined as follows:

$$SCG = ij \in EG1di + dj$$

[iv] The result derived through the application of Definition 4 is outlined below:

$SC(KB) = 413+2 \times 14+4 \times 14+6 \times 15+1 \times 16+4 \times 16+3 \times 17$

$SC(KB)\ 4 \times 0.5774 + 2 \times 0.5 + 4 \times 0.5 + 6 \times 0.4472 + 1 \times 0.4082 + 4 \times 0.4082 + 3 \times 0.3779 = 11.168.$

Definition 5. The geometric–arithmetic (GA) index was introduced by Vukićević and Furtula, drawing inspiration from the Randić

connectivity index. In their work, they also established both upper and lower bounds for the GA index and identified that the star graph and path graph correspond to the minimum and maximum GA values, respectively [62]. This modified GA index is now commonly used to predict various physical properties of chemical structures and is defined as follows:

$$GA\ G = ij \in E(G) 2di \times djdi + dj$$

[v] The result derived through the application of Definition 5 is outlined below:

$$GA(KB) = 421 \times 23+2 \times 21 \times 34+4 \times 22 \times 24+622 \times 35+1 \times 22 \times 46+4 \times 23 \times 36+3 \times 23 \times 47$$
$$= 4 \times 0.9428 + 2 \times 1.7321 + 4 \times 1.0 + 6 \times 1.0954 + 1 \times 0.9428 + 4 \times 1.0 + 3 \times 0.9903 = 23.294$$

Definition 6. The Harmonic index, sometimes considered a variant of the Randic index, was first introduced by Favaron et al. It serves as an important topological descriptor for predicting physical properties of molecular structures [63]. The modified Harmonic index H(G) is defined as follows:

$$HG = ij \in E(G) 2di + dj$$

[vi] The result derived through the application of Definition 6 is outlined below:

$$H(KB) = 423+2 \times 24+4 \times 24+6 \times 25+1 \times 26+4 \times 26+3 \times 27$$
$$H(KB) = 2.6667 + 1 + 2 + 2.4 + 0.3333 + 1.3333 + 0.857 = 10.590$$

Definition 7. The third Zagreb index, originally introduced by Gutman et al. over four decades ago, has since inspired the development of several alternative forms of this topological descriptor [64,65]. One such variation is defined as follows:

$$ZG3(G) = ij \in E(G) di - dj$$

[vii] The result derived through the application of Definition 7 is outlined below:

$$ZG_3\ (KB) = 41\text{-}2+2 \times 1\text{-}3+4 \times 2\text{-}2+6 \times 2\text{-}3+1 \times 2\text{-}4+4 \times 3\text{-}3+3 \times 3\text{-}4$$
$$ZG_3\ (KB) = 4 \times 1 + 2 \times 2 + 4 \times 0 + 6 \times 1 + 1 \times 2 + 4 \times 0 + 3 \times 1 = 19$$

Definition 8. The second Hyper-Zagreb index is a degree-based topological index that effectively captures key molecular characteristics. The HM_2 index has been studied across various graph structures, and several bounds have been established. Moreover, literature reports have explored linear regression analyses linking degree-based indices with physical properties, such as the boiling points of benzenoid hydrocarbons [66,67]. The second Hyper-Zagreb index $HM_2(G)$is defined as follows:

$$HM2G = ij \in E(G)(di + dj)2$$

[viii] The result derived through the application of Definition 8 is outlined below:

$$HM_2(KB) = 432+2 \times 42+442+6 \times 52+1 \times 62+4 \times 62+3 \times 72$$
$$HM_2(KB) = 609$$

Definition 9. The Forgotten index (F-index), introduced by Furtula and Gutman, shares a close relationship with the first Zagreb index. This topological index plays a crucial role in estimating chemical stability and assessing the pharmacological potential of novel drug-like molecules [68,69]. The F-index of a graph F(G) is defined as follows:

$$FG = ij \in E(G)[(di)2 + (dj)2]$$

[ix] The result derived through the application of Definition 9 is outlined below:

$$F(KB) = 4 \times (12+22)+2 \times (12+32)+4 \times (22+22)+6 \times (22+32)+1 \times (22+42)+4 \times (32+32)+3 \times (32+42)$$
$$F(KB) = 20 + 20 + 32 + 78 + 20 + 72 + 75 = 317$$

Definition 10. Several decades ago, Vukicevic and Gasperov introduced a novel class of biological descriptors known as the symmetric division degree (SDD) topological index. This index provides meaningful insights into molecular structures and their biological properties [70]. The symmetric division degree index of a graph, denoted as SSD(G)is defined as follows:

$$SSDG = ij \in E(G) di2 + dj2\ didj$$

[x] The result derived through the application of Definition 10 is outlined below:

$$SSD(KB) = 41+42+2 \times 1+93+4 \times 4+44+6 \times 4+96+1 \times 4+168+4 \times 9+99+3 \times 9+1612$$
$$SSD(KB) = 10 + 6.6667 + 8 + 13 + 2.5 + 8 + 6.25 = 54.417$$

The ten degree-based topological indices of the molecular graph Kojibiose (KB) are

$$\chi(KB) = 10.986,\ M_1\ (KB) = 117,\ M_2\ (KB) = 146,\ ABC(KB) = 16.843,\ SC(KB) = 11.168$$
$$GA(KB) = 23.294,\ H(KB) = 10.590,\ ZG_3\ (KB) = 19,\ HM_2(KB) = 609,\ F(KB) = 317$$

Hence, the molecular structure of Kojibiose (KB) was evaluated as a graph Fig. 1 and a range of degree-based topological indices to understand its structural and pharmacological properties. By representing the KB molecule through its hydrogen-depleted graph, we computed ten significant topological descriptors. The calculated values provide a comprehensive mathematical fingerprint of the molecular architecture of Kojibiose, allowing us to draw correlations between structure and potential biological activity. Notably, the high value of the second Hyper-Zagreb index ($HM_2 = 609$) and the Forgotten index ($F = 317$) indicate a stable and pharmacologically significant molecular framework. These findings demonstrate that topological descriptors serve as efficient computational tools in quantitative structure–activity/property relationship (QSAR/QSPR) studies, supporting the theoretical prediction of chemical reactivity and therapeutic potential.

5. Conclusion

By identifying KB as a multifunctional molecule by a combined analysis of its electronic structure, nonlinear optical properties, and antibacterial efficacy, this work goes beyond previous biological investigations. Quantum chemical calculations based on DFT have confirmed that KB has a well-optimized molecular structure with bond lengths, angles, and hydrogen bonding patterns typical of stable disaccharides. Strong donor–acceptor interactions and intramolecular charge delocalization are highlighted by the NBO analysis, and these features are consistent with the chemical stability that has been observed. The high hyperpolarizability and polarizability values imply that KB is a viable candidate for nonlinear optical (NLO) applications, while the UV-Vis and HOMO-LUMO analyses show effective electronic transitions. In experiments, KB showed significant antibacterial activity against S. aureus and E. coli, indicating that it has the potential to be a

broad-spectrum antibacterial agent. Its inhibitory effect is probably facilitated by the presence of multiple hydroxyl groups, which strengthen hydrogen bonds with bacterial cell components. Together with its advantageous NLO characteristics and electronic stability, KB shows promise as a bioactive molecule that can be used as a therapeutic antibacterial agent and as a material of interest for photonic and opto-electronic applications.

CRediT authorship contribution statement

Jeffrin JA Laura: Writing – original draft, Methodology, Investigation. **P. Rajesh:** Writing – original draft, Supervision. **S. Kayashrini:** Writing – review & editing, Software, Formal analysis. **S Bala Abirami:** Software, Formal analysis.

Declaration of competing interest

The authors declare that they have no known competing financial interests or personal relationships that could have appeared to influence the work reported in this paper.

Data availability

Data will be made available on request.

References

[1] Marina Díez-Municio, Antonia Montilla, F.Javier Moreno, Miguel Herrero, A sustainable biotechnological process for the efficient synthesis of kojibiose, Green Chem. 4 (2014), https://doi.org/10.1039/C3GC42246A.

[2] Keya Mukherjee, Tamari Narindoshvili, Frank M. Raushel, Discovery of a Kojibiose Phosphorylase in *Escherichia coli* K-12, J. Biol. Chem. 57 (2018), https://doi.org/10.1021/acs.biochem.8b00392.

[3] Mattias U. Roslund, Petri Tähtinen, Matthias Niemitz, Rainer Sjöholma, Complete assignments of the 1H and 13C chemical shifts and $J_{H,H}$ coupling constants in NMR spectra of D-glucopyranose and all D-glucopyranosyl-D-glucopyranosides, Carbohydr. Res. 343 (2008), https://doi.org/10.1016/j.carres.2007.10.008.

[4] Júlia Capp Zilles, Francielli Lima dos Santos, Irene Clemes Kulkamp-Guerreiro, Renata Vidor Contr, Biological activities and safety data of kojic acid and its derivatives: A review, Exp. Dermatol. 10 (2022), https://doi.org/10.1111/exd.14662.

[5] Gulşah Karakayaa, Aslı Tureb, Ayşe Ercanc, Selin Onculc, Mutlu Dilsiz Aytemira, Synthesis, computational molecular docking analysis and effectiveness on tyrosinase inhibition of kojic acid derivatives, Bioorg. Chem. 88 (2019), https://doi.org/10.1016/j.bioorg.2019.102950.

[6] M.J. Frisch, G.W. Trucks, H.B. Schlegel, G.E. Scuseria, M.A. Robb, J.R. Cheese-man, G. Scalmani, V. Barone, B. Mennucci, G.A. Petersson, H. Nakatsuji, M. Caricato, X. Li, H.P. Hratchian, A.F. Izmaylov, J. Bloino, G. Zheng, J.L. Son-nenberg, M. Hada, M. Ehara, K. Toyota, R. Fukuda, J. Hasegawa, M. Ishida, T. Nakajima, Y. Honda, O. Kitao, H. Nakai, T. Vreven, J.A. Montgomery Jr., J.E. Peralta, F. Ogliaro, M. Bearpark, J.J. Heyd, E. Brothers, K.N. Kudin, V.N. Staroverov, R. Kobayashi, J. Normand, K. Raghavachari, A. Rendell, J.C. Bu-rant, S.S. Iyengar, J. Tomasi, M. Cossi, N. Rega, J.M. Millam, M. Klene, J.E. Knox, J.B. Cross, V. Bakken, C. Adamo, J. Jaramillo, R. Gomperts, R.E. Stratmann, O. Yazyev, A. J. Austin, R. Cammi, C. Pomelli, J.W. Ochterski, R.L. Martin, K. Mo-rokuma, V. G. Zakrzewski, G.A. Voth, P. Salvador, J.J. Dannenberg, S. Dapprich, A.D. Daniels, O. Farkas, J.B. Foresman, J.V. Ortiz, J. Cioslowski, D.J. Fox, Gaussian 09, Revision E.01, Gaussian, Inc., Wallingford CT, 2009.] program together with 6-31G(d,p) basis set function of the density functional theory (DFT) utilizing gradient geometry optimization [H.B. Schlegel, J. Comput. Chem. 3 (1982) 214–218.

[7] A. Frisch, A.B. Nielsen, A.J. Holder, Gaussview Users Manual, Gaussian Inc., Pittsburg, PA, 2000.

[8] M.H. Jamroz, Vibrational Energy Distribution Analysis, 4, VEDA, Warsaw, 2004.

[9] Tian Lu, Feiwu Chen, Multiwfn: A multifunctional wavefunction analyzer, J. Comput. Chem. 33 (2012) 580–592, https://doi.org/10.1002/jcc.22885.

[10] G.M. Morris, D.S. Goodsell, R.S. Halliday, R. Huey, W.E. Hart, R.K. Belew, A. J. Olson, Automated docking using a lamarckian genetic algorithm and empir- ical binding free energy function, J. Comput. Chem. 19 (1998) 1639–1662, https://doi.org/10.1002/(SICI)1096-987X(19981115)19:14<1639::AID-JCC10>3.0.CO;2-B.

[11] R.G. Parr, L.v. Szentpály, S. Liu, Electrophilicity index, J. Am. Chem. Soc. 121 (1999) 1922–1924, https://doi.org/10.1021/ja983494x.

[12] P. Geerlings, F. De Proft, W. Langenaeker, Conceptual density functional theory, Chem. Rev. 103 (2003) 1793–1874, https://doi.org/10.1021/cr990029p.

[13] T. Koopmans, Über die Zuordnung von Wellenfunktionen und Eigenwerten zu den einzelnen Elektronen eines Atoms, Physica 1 (1934) 104–113, https://doi.org/10.1016/S0031-8914(34)90011-2.

[14] Sibel Celik, DFT investigations and molecular docking as potent inhibitors of SARS-CoV-2 main protease of 4-phenylpyrimidine, J. Mol. Struct. 1277 (2023), https://doi.org/10.1016/j.molstruc.2022.134895.

[15] D. Jacquemin, I. Duchemin, X. Blase, Benchmarking the accuracy of TD-DFT for UV–Vis absorption spectra, J. Chem. Theory Comput. 11 (2015) 5340–5359, https://doi.org/10.1021/acs.jctc.5b00777.

[16] A.D. Laurent, D. Jacquemin, TD-DFT benchmarks for absorption spectra: role of solvent and functional effects, Int. J. Quantum Chem. 116 (2016) 1003–1013, https://doi.org/10.1002/qua.25175.

[17] A. Alfind Paul Frit, Hemant S. Deshmukh, Rahul A. Shinde, Vishnu A. Adole, Triazolyl-Pyridinyl-Thiazole Molecular Hybrids: Synthesis, Spectral Characterization, Structural Analysis, DFT Calculations, Antitubercular Potential, Molecular Docking and Pharmacokinetic Evaluation, J. Mol. Struct. 1348 (2025), https://doi.org/10.1016/j.molstruc.2025.143471.

[18] M.C. Almandoz, M.I. Sancho, P.R. Duchowicz, S.E. Blanco, UV–Vis spectroscopic study and DFT calculation on the solvent effect of trimethoprim in neat solvents and aqueous mixtures, Spectrochim. Acta A 129 (2014) 52–60, https://doi.org/10.1016/j.saa.2014.02.191.

[19] M.E. Casida, Time-dependent density functional response theory for molecules, J. Mol. Struct. (THEOCHEM) 914 (2009) 3–18, https://doi.org/10.1016/j.theochem.2009.08.020.

[20] N. Gunaya, O. Tamerb, D. Avcı, E. Tarcan, Y. Atalay, Molecular modelling, spectroscopic characterization and nonlinear optical analysis on N-Acetyl-DL-methionine, Rev. Mex. Fis 66 (2020), https://doi.org/10.31349/RevMexFis.66.749.

[21] Mehmet Karabacak, Etem Kose, Ahmet Atac, Abdullah M. Asiri, Mustafa Kurt, Monomeric and dimeric structures analysis and spectroscopic characterization of 3,5-difluorophenylboronic acid with experimental (FT-IR, FT-Raman, 1 H and 13C NMR, UV) techniques and quantum chemical calculations, J. Mol. Struct. 1058 (2014) 79–96, https://doi.org/10.1016/j.molstruc.2013.10.064.

[22] U. Unsalan, O. Gülseren, A. Deniz, I. Uzun, E. Tüzün, FT-IR spectral, DFT studies and detailed vibrational assignments of a novel molecule using PED analysis, Spectrochim Acta A Mol. Biomol. Spectrosc 92 (2012) 25–34, https://doi.org/10.1016/j.saa.2012.08.050.

[23] T. Hong, Q. Liu, X. Zhang, Applications of infrared spectroscopy in polysaccharide analysis: Enabling DFT-based assignment of vibrational signatures, Carbohydr. Polym. 255 (2021) 117–123, https://doi.org/10.1016/j.fochx.2021.100168.

[24] J.W. Cao, H.J. Li, Z. Qin, DFT investigations of the vibrational spectra and infrared assignments of ice II: Combined normal-mode analysis and comparison with experimental INS, IR & Raman, Molecules 24 (17) (2019) 3135, https://doi.org/10.3390/molecules24173135.

[25] B. Gieroba, K. Malinowska, Application of vibrational spectroscopic techniques in the study of polysaccharides: Emphasis on FT-IR, DFT and mode assignment, Polymers 15 (4) (2023) 987, https://doi.org/10.3390/ijms24032630.

[26] Y. Ji, K. Huang, W. Xu, DFT-Calculated IR spectrum of amide I, II, and III bands: Vibrational assignment of N-methylacetamide by B3LYP/6-311++G(d,p), ACS Omega 5 (30) (2020) 19562–19572, https://doi.org/10.1021/acsomega.9b04421.

[27] N. Takahashi, E. Fukushi, S. Onodera, N. Benkeblia, T. Nishimoto, J. Kawabata, N. Shiomi, Three novel oligosaccharides synthesized using Thermoanaerobacter brockii kojibiose phosphorylase, Chem. Cent. J. 1 (2007) 1–7, https://doi.org/10.1186/1752-153X-1-18.

[28] H. Chaen, T. Nishimoto, T. Nakada, S. Fukuda, M. Kurimoto, Y. Tsujisaka, Enzymatic synthesis of novel oligosaccharides from L-sorbose, maltose, and sucrose using kojibiose phosphorylase, J. Biosci. Bioeng. 92 (2) (2001) 173–176, https://doi.org/10.5458/jag.jag.JAG-2018_0002.

[29] K. Chiku, M. Wada, H. Atsuji, A. Hosonuma, M. Yoshida, H. Ono, M. Kitaoka, Epimerization and decomposition of kojibiose and sophorose by heat treatment under neutral pH conditions, J. Appl. Glycosci. 66 (1) (2019) 1–9, https://doi.org/10.1021/acs.biochem.8b00392.

[30] T. Yamamoto, H. Yamashita, K. Mukai, H. Watanabe, M. Kubota, H. Chaen, S. Fukuda, Construction and characterization of chimeric enzymes of kojibiose phosphorylase and trehalose phosphorylase from Thermoanaerobacter brockii, Carbohydr. Res. 341 (14) (2006) 2350–2359, https://doi.org/10.1016/j.carres.2006.06.024.

[31] A. Kawano, K. Fukui, Y. Matsumoto, A. Terada, A. Tominaga, N. Nikaido, T. Tonozuka, K. Totani, N. Yasutake, Analysis of transglucosylation products of Aspergillus niger α-glucosidase that catalyzes the formation of α-1, 2-and α-1, 3-linked oligosaccharides, J. Appl. Glycosci. 67 (2) (2020) 41–49, https://doi.org/10.5458/jag.jag.JAG-2019_0015.

[32] Mohd Faizan, Ahmad Sheeraz, Mohammad Bhat, Jane Alam, Ziya Afroz, Shabbir Ahmad, Anharmonic vibrational and electronic spectral study of 2-amino-4- hydroxy-6emethylpyrimidine: A combined experimental (FTIR, FT-Raman, UV -Vis) and theoretical (DFT, MP2) approach, J. Mol. Struct. (2017) 1148, https://doi.org/10.1016/j.molstruc.2017.07.007.

[33] A. Jumabaev, B. Khudaykulov, S.J. Koyambo-konzapa, U. Holikulov, H. Hushvaktov, A. Absanov, I. Doroshenko, Exploring Noncovalent Interactions Of Thiophene-2-Carboxylic Acid In Ethanol Via Vibrational Spectroscopy And DFT Calculations, Ukr. J. Phys. 70 (2025), https://doi.org/10.15407/ujpe70.6.391.

[34] Vishnu A. Adole, Ravindra H. Waghchaure, Thansing B. Pawar, Bapu S. Jagdale, Kailas H. Kapadnis, Synthesis, Molecular Structure, HOMO-LUMO and Spectroscopic Investigation of (*E*)-1-(2,4-Dichloro-5-fluorophenyl)-3- (2,6-dichlorophenyl)prop-2-en-1-one: A DFT Based Computational Exploration, Asian J. Org. Chem. 5 (2020), https://doi.org/10.14233/ajomc.2020.AJOMC-P285.

[35] Vishnu Ashok Adole, Bapu Sonu Jagdale, Thansing Bhavsing Pawar, Bhatu Shivaji Desale, Molecular Structure, Frontier Molecular Orbitals, MESP and UV–Visible Spectroscopy Studies of Ethyl 4-(3,4-dimethoxyphenyl)-6-methyl-2-

oxo-1,2,3,4-tetrahydropyrimidine-5-carboxylate: A Theoretical and Experimental Appraisal, Mat. Sci. Res. India 17 (2020). https://www.researchgate.net/publication/343373983.
[36] Hilal Nur Yogurtcu, Cem Cuneyt Ersanlı, Structural Parameters, NLO, HOMO, LUMO, MEP, Chemical Reactivity Descriptors, Mulliken-NPA, Thermodynamic Functions, Hirshfeld Surface Analysis and Molecular Docking of 1,3-Bis(4-methylphenyl) triazine, ISVOS J. 9 (2025), https://doi.org/10.47897/bilmes.1697802.
[37] Cem Cuneyt Ersanl, Sultan Basak, A Multidimensional Investigation from Electronic Properties to Biological Activity of 2-[(4-Hydroxyphenyl) iminomethyl] thiophene by DFT, HOMO-LUMO, MEP, NLO, NBO, Mulliken, Hirshfeld and Molecular Docking Analyses, ISVOS J. 9 (2025), https://doi.org/10.47897/bilmes.1704235.
[38] Sk. Hussain Basha, Srinivasadesikan Venkatesan, Imidazolium Ionic Liquid with Graphene and Graphene Oxide for Water Splitting Applications: A DFT Study, CON-282(2025) https://www.researchgate.net/publication/393149806.
[39] Semiha Bahceli, Ebru Karakaş Sarıkaya, Omer Dereli, Photovoltaic performance of 4Cyano3fluorobenzaldehyde: spectroscopic (FTIR, 1H and 13CNMR, FTRaman, and UV–vis.) and DFT studies, Res. Chem. Intermed. 51 (2025), https://doi.org/10.1007/s11164-025-05564-x.
[40] E. Eunice, Johanan Christian Prasana, Alzheimer's Dementia Targeting by Plant-Derived 2,6-Dimethoxybenzoic Acid: *In vitro*, DFT and Molecular Docking Study, Asian J. Chem. 37 (2025), https://doi.org/10.14233/ajchem.2025.33504.
[41] Karthikeyan Asokan, Sumathi Sivaraman, Karthik Nallasamy, Jeyavijayan Subbiah and Selvarengan Paranthaman, Spectroscopic study, Quantum Chemical Investigations, *In silico* and Drug Likeness of 4-Chloro-6,7-dimethoxyquinazoline: A potent study of new anti-alzheimer agent, Indian J. Biochem. Biophys. 62 (2025), https://doi.org/10.56042/ijbb.v62i4.14277.
[42] B. Sumathi, C.P. Devipriya, V. Sabar, M. Aravinthraj, P. Muzammil, J. Udayaseelan, Exploring the Structural, electronic, binding and thermal properties of 4- (4-Fluorophenyl) -6-Isopropyl-2-(N-Methyl-N-Methanesulfonylamino)-5-Pyrimidine Carboxaldehyde: DFT and Molecular Docking Approach, Res. Sq. 1 (2025), https://doi.org/10.21203/rs.3.rs-6734711/v1.
[43] Abduvakhid Jumabaev, H. Hushvaktov, A. Absanov, Bekzod Khudaykulov, Zokhid Ernazarov, Leonid Bulavin, Vibrational Spectra and Computational Study of Amyl Acetate: MEP, AIM, RDG, NCI, ELF and LOL Analysis, Ukr. J. Phys. 69 (2024), https://doi.org/10.15407/ujpe69.10.742.
[44] Sakshi Gupta, Sandhya Savita, Ajay Prakash, Tahmeena Khan, Kulsum Hashmi Satya, Seema Joshi, Synthesis, DFT and Molecular docking studies in search of antimicrobial activity of (E)-4-((2-carbamothioylhydrazineylidene) methyl) benzoic acid, J. Mol. Struct. 1293 (2023), https://doi.org/10.1016/j.molstruc.2023.136276.
[45] A. Jumabaev, B. Khudaykulov, S.J. Koyambo-Konzapa, U. Holikulov, H. Hushvaktov, A. Absanov, I. Doroshenko, Exploring Noncovalent Interactions Of Thiophene-2-Carboxylic Acid In Ethanol Via Vibrational Spectroscopy and DFT Calculations, Ukr. J. Phys. 70 (2025), https://doi.org/10.15407/ujpe70.6.391.
[46] I. Shafiq, N. Raza, S. Dildar, et al., Unraveling the NLO potential of isoquinoline functionalized chromophores via molecular modeling using DFT/TD-DFT approaches, Sci. Rep. 15 (2025) 23236, https://doi.org/10.1038/s41598-025-04911-7.
[47] D.S. Arora, J. Kaur, Antibacterial activity of some phenolic compounds against Gram-positive and Gram-negative bacteria, Indian J. Exp. Biol. 57 (6) (2019) 403–410.
[48] CLSI, Performance standards for antimicrobial susceptibility testing, 30th ed., Clinical and Laboratory Standards Institute, 2020.
[49] S. Mandal, M. Mandal, N.K. Pal, Evaluation of antibacterial activity of carbohydrates and their derivatives, IJPSRR 24 (2) (2014) 45–49.
[50] F. Nazzaro, F. Fratianni, L. De Martino, R. Coppola, V. De Feo, Effect of essential oils on pathogenic bacteria, Pharmaceuticals 6 (12) (2013) 1451–1474, https://doi.org/10.3390/ph6121451.
[51] Francisco Santos, Carlos Cardoso, Rodrigues Jr, Boni Jose, Leonardo, Luis Abegão, Nonlinear Optical Materials: Predicting the First-Order Molecular Hyperpolarizability of Organic Molecular Structures, Photonics 10 (5) (2023), https://doi.org/10.3390/photonics10050545, 2023.
[52] Karakaş Sarıkaya, Ekincioğlu Ebru, Bahçeli Yavuz, Semiha, Ömer Dereli, Analysis of the nonlinear optical properties, vibrational spectra, DFT method and photovoltaic performance of cyanidin-3-rutinoside chloride, Opt. Quantum Electron. 56 (8) (2024), https://doi.org/10.1007/s11082-024-07294-7.
[53] A. Irfan, A.G. Al-Sehemi, First-principles investigation of nonlinear optical properties of organic materials, Optik 181 (2019) 11–18, https://doi.org/10.1016/j.ijleo.2018.12.002.
[54] M. Khalid, First-principles study of electronic and nonlinear optical properties of organic NLO materials: role of intramolecular charge transfer, RSC Adv. 10 (2020) 17475–17490, https://doi.org/10.1039/D0RA02857F.
[55] Naga Kothoori, Pandiyan Sivasakthi, Mallesham Baithy, Ramprasad Misra, Pralok Samanta, Rational design and investigation of nonlinear optical response properties of pyrrolopyrrole aza-BODIPY-based novel push–pull chromophores, RSC Adv., 14 (22) (2024) 15560–15570, https://doi.org/10.1039/d4ra02861a.
[56] Mubashar Ilyas, Maroof Ahmad Khan, Lin Xiong, Li Zhang, Muhammad Lauqman, Muhammad Abbas, Hafiz Muhammad Zohaib, Nagesh Manurkar, Hui Li, Enhancements of the first and second hyperpolarizability of a GMP coordination polymer: crystal structure and computational studies, Dalton Trans 54 (2025) 5921–5934, https://doi.org/10.1039/D5DT00248F.
[57] M. Lawrence, P. Rajesh, M. Thirunavukkarasu, S. Muthu, Solute-solvent interactions, electrostatic & covalent surface analysis, and pharmacokinetic studies via in-silico simulation on diethyl 3-hydroxyglutarate: Anti-hypercholesterolemia activity, J. Mol. Liquids 382 (2023) 121940, https://doi.org/10.1016/j.molliq.2023.121940.
[58] B. Deepa, C. Natarajan, R. Vignesh, Muhammad KS, QSPR analysis of anti-asthmatic drugs using some new distancebased topological indices: a comparative study, Int. J. Quantum Chem. 124 (2024), https://doi.org/10.1002/qua.27372.
[59] A.S. Jeyamangala, K.R.S. Angelin, K.S. Muhammad, J.Z. Tariq, Computation of degree-based topological indices for the complex structure of ruthenium bipyridine, Int. J. Quantum Chem. 124 (2024), https://doi.org/10.1002/qua.27310.
[60] K. Zunaira, Z. Shahid, U. Asad, K.S. Muhammad, B.B. Melaku, Computation of molecular description of supramolecular Fuchsine model useful in medical data, Sci Rep 10933 (2024), https://doi.org/10.1038/s41598-024-60284-3.
[61] B. Sergio, EN & Juan, R. Juan, Extremal trees for the Randic index with given domination number, Appl. Math. Comput. 375 (2020), https://doi.org/10.1016/j.amc.2020.125122.
[62] G. Modjtaba, A.H. Mohammad, A new version of Zagreb indices, Filomat 26 (2012), https://doi.org/10.2298/FIL1201093G.
[63] M.Z. Xiu, Q.S. Yu, W. Hua, Xiao DZ, On the ABC index of connected graphs with given degree sequences, J. Math. Chem. 56 (2018), https://doi.org/10.1007/s10910-017-0802-4.
[64] M.A. Abeer, M. Emina, A. Akbar, General Atom-Bond Sum- Connectivity Index of Graph, Mathematics 11 (2023), https://doi.org/10.3934/math.20231210.
[65] Y. Yan, Z. Bo, T. Nenad, On geometric-arithmetic index, J. Math. Chem. 47 (2010), https://doi.org/10.1007/s10910-009-9603-8.
[66] Z. Lingping, The harmonic index for graphs, Appl. Math. Lett. 25 (2012), https://doi.org/10.1016/j.aml.2011.09.059.
[67] G. Modjtaba, A.H. Mohammad, The third version of Zagreb Index, Discret. Math. Algor. Appl. 5 (2013), https://doi.org/10.1142/S1793830913500390.
[68] Y. Guofeng, K.S. Muhammad, H. Mazhar, H. Nazir, S. Zohaib, B.P. Fikre, On topological indices and entropy measures of beryllonitrene network via logarithmic regression model, Sci. Rep. 7187 (2024), https://doi.org/10.1038/s41598-024-57601-1.
[69] G. Wei, K.S. Muhammad, I. Muhammad, K.J. Muhammad, R.F. Mohammad, Forgotten topological index of chemical structure in drugs, Saudi Pharm. J. 24 (2016), https://doi.org/10.1016/j.jsps.2016.04.012.
[70] M.C. Shanmukha, N.S. Basavarajappa, K.C. Shilpa, A. Usha, Degree-based topological indices on anticancer drugs with QSPR analysis, Heliyon 6 (2020), https://doi.org/10.1016/j.heliyon.2020.e04235.